Parameterizing mesoscale eddy buoyancy transport over sloping topography

Aleksi Nummelin[1,2,3], **Pål Erik Isachsen**[1,4]

[1]University of Oslo, Department of Geosciences, Oslo, Norway
[2]NORCE Norwegian Research Centre AS and Bjerknes Centre for Climate Research, Bergen, Norway
[3]Finnish Meteorological Institute, Helsinki, Finland
[4]Norwegian Meteorological Institute, Oslo, Norway

Key Points:

- Eddy buoyancy diffusivity reduction over bottom slopes can be parameterized using the Eady growth rate and topographic Rhines scale.
- Realistic reduction in buoyancy diffusivity in a coarse resolution model enhances baroclinic boundary currents.
- A topographically-aware eddy efficiency factor improves the parameterization and further reduces biases in global simulations.

Corresponding author: Aleksi Nummelin, `aleksi.nummelin@fmi.fi`

Abstract

Most of the ocean's kinetic energy is contained within the mesoscale eddy field. Models that do not resolve these eddies tend to parameterize their impacts through down-gradient transport of buoyancy and tracers, aiming to reduce the large-scale available potential energy and spread tracers. However, the parameterizations used in the ocean components of current generation Earth System Models (ESMs) rely on an assumption of a flat ocean floor even though observations and high-resolution modelling show that eddy transport is sensitive to the potential vorticity gradients associated with a sloping sea floor. We show that buoyancy diffusivity diagnosed from idealized eddy-resolving simulations is indeed reduced over both prograde and retrograde bottom slopes (topographic wave propagation along or against the mean flow, respectively) and that the reduction can be skilfully captured by mixing length parameterization by introducing the topographic Rhines scale as a length scale. This modified 'GM' parameterization enhances the strength of thermal wind currents over the slopes in coarse-resolution, non-eddying, simulations. We find that in realistic global coarse-resolution simulations the impact of topography is most pronounced at high latitudes, enhancing the mean flow strength and reducing temperature and salinity biases. Reducing buoyancy diffusivities further with a mean-flow dependent eddy efficiency factor has notable effects also at lower latitudes and leads to reduction of global mean biases.

Plain Language Summary

Due to their high computational costs, global climate models are usually run at coarse spatial resolution, which does not allow them to resolve the ocean weather—mesoscale eddies—which are an important part of the ocean energy cycle and contribute to mixing of tracers such as heat and carbon. Eddies are instead parameterized in an idealized manner which relates the eddy-driven transport to the strength of the vertical and horizontal density gradients in the ocean. Such parameterization do not take into account impacts of large-scale bottom bathymetry which have been shown to weaken the eddy driven transport. Here we use high-resolution eddy-resolving simulations to improve existing parameterizations so that they become sensitive to the bottom slope. We show that such a parameterization qualitatively captures the transport reduction seen in idealized high-resolution simulations and can also reduce errors in realistic global simulations.

1 Introduction

At present, the ocean components of most global climate models are used at resolutions that require parameterizing the oceanic mesoscale (Fox-Kemper et al., 2019). And although coupled simulations with eddying ocean fields are slowly emerging (Chang et al., 2020), mesoscale eddy parameterizations are still likely part of ocean models for another decade. Most present-day parameterizations have their origins in the works of Gent and Mcwilliams (1990); Gent et al. (1995) and Redi (1982), tackling eddy-induced advection and tracer mixing, respectively. The 'GM' advection is cast in terms of a horizontally down-gradient and vertically up-gradient buoyancy diffusion which acts to reduce available potential energy. And 'Redi' diffusion mixes tracers down-gradient along isopycnals (Gent, 2011). In practice, most model implementations focus on estimating an eddy diffusion coefficient, or eddy diffusivity, which is then used to drive both eddy induced advection and mixing. It is generally understood that these are separate processes. However, previous studies have suggested that GM and Redi coefficients differ only in their vertical structure (K. S. Smith & Marshall, 2009; Abernathey et al., 2013; Bachman et al., 2020) and, therefore, that their depth-averaged values should be similar up to a constant factor.

Depth-averaged eddy diffusion coefficients in coarse-resolution climate models are often parameterized following mixing length theory, set proportional to the product of some eddy velocity scale and a mixing length scale. Some work has gone into estimating the eddy velocity scale by implementing a prognostic equation for eddy energy (Eden & Greatbatch, 2008; Marshall et al., 2012; Mak et al., 2018; Bachman, 2019; Jansen et al., 2019), but this is still very much an active field of research. The study by Visbeck et al. (1997) therefore continues to influence the practical use of the mixing length approach. Drawing on earlier works by Green (1970) and Stone (1972), the authors proposed that the velocity scale be based on the product of the growth rate of baroclinic instability in the linearized Eady model (Eady, 1949) and some length scale. Assuming that the mixing length is also set by the same scale, the diffusivity will then scale as the Eady growth rate and the square of the length scale. Visbeck et al. (1997) associated the mixing length with the 'width of the baroclinic zone' which they defined as "the width of the region where the local growth rate exceeds 10% of the maximum growth rate of the field". The concept, however, is hard to define in any but the the most idealized model geometries, and length scales therefore need to be formed from theoretical dynamical arguments.

As proposed by Stone (1972), one obvious candidate for length scale is the internal deformation radius, the approximate scale of fastest unstable growth in the Eady model. Solid observational evidence for the relevance of this length scale has been presented by Stammer (1997) and Eden (2007). However, other relevant scales arise if dynamics beyond the Eady framework is accounted for, most notably bottom friction and internal potential vorticity (PV) gradients. Jansen et al. (2015), for example, examined the role of bottom friction and the planetary vorticity gradient in a two-layer flat-bottom channel model. They found that bottom friction primarily influences the vertical distribution of eddy energy and that the mixing length in most of their simulations is set by the Rhines scale, i.e. the transition scale between nonlinear and linear PV dynamics on the flat-bottom planetary beta plane (Rhines, 1977). More generally, Jansen et al. (2015) found that in order to cover various dynamical regimes, the smaller of several candidate length scales should be chosen. And, in fact, the observational studies of both Stammer (1997) and Eden (2007) specifically pointed to a minimum of the internal deformation radius and the Rhines scale as a best fit for eddy length scales over much of the world oceans.

These principles remain the standard in state-of-the-art models, although development has occurred in later years. As mentioned above, there has been extensive focus on developing prognostic equations for eddy energy. And a considerable effort has gone into studying effects of horizontal eddy anisotropy (R. D. Smith & Gent, 2004) and the suppression of mixing across strong mean flows (Ferrari & Nikurashin, 2010; Klocker et al., 2012, and references therein). It's worth noting, however, that most of the development up until recently has been guided by observed dynamics in low- and mid-latitudes. Current parameterizations thus lack any treatment of two aspects that are potentially of huge importance in high latitude oceans, namely the presence of sea ice and the potential vorticity gradients imposed by sloping bottom topography. A sea ice cover can effectively have the same influence as bottom friction on both growth of baroclinic instability as well as dissipation of existing mesoscale and sub-mesoscale eddies (Meneghello et al., 2021). But this topic will be left out from the present study. We will instead focus on the dynamical impacts of bottom slopes, i.e. continental slopes and mid-ocean ridge systems, whose imprints can be easily seen in observations of both mean currents and mesoscale energy fields, especially at high northern latitudes (Nøst & Isachsen, 2003; Koszalka et al., 2011; Trodahl & Isachsen, 2018). Such imprints of topographic PV gradients can also be seen at lower latitudes, e.g. in drifter and float paths (LaCasce, 2000; Fratantoni, 2001).

Sloping bottom topography can suppress growth rate and reduce length scales of baroclinic instability (e.g. Blumsack & Gierasch, 1972; Mechoso, 1980; Isachsen, 2011; Brink, 2012) as well as impact finite-amplitude eddy fields (e.g. Bretherton & Haidvogel, 1976; Vallis & Maltrud, 1993; Lacasce & Brink, 2000; K. Stewart et al., 2015; Wang & Stewart, 2018). To this end, new topography-aware parameterizations have started to emerge, both for eddy-induced advection and isopycnal mixing. In particular, Wang and Stewart (2020) and Wei et al. (2022) used high-resolution model simulations of flows over idealized continental slopes in a re-entrant channel to test different scaling relations for the GM diffusivity. The two works examined eddy characteristics and fluxes across retrograde and prograde mean currents, respectively, meaning currents that are in the opposite and same direction as topographic waves. Both studies diagnosed the eddy energy from the high-resolution fields and used this to examine traditional mixing length formulations in addition to the 'GEOMETRIC' formulation of Marshall et al. (2012) which is based on eddy energy and the inverse of the Eady growth rate. In general, the two formulations performed similarly, suggesting that a good knowledge of the eddy energy field is key. But, importantly, both studies also found that empirical prefactors that depend on the topographic slope are needed to reproduce the very weak eddy buoyancy fluxes across sloping bottom topography.

Wei and Wang (2021) carried on from Wang and Stewart (2020), but focused on the along-isopycnal tracer (Redi) diffusivity—in retrograde flows only. The authors scaled the Redi diffusivity from (the square root of) the diagnosed eddy kinetic energy and the internal deformation radius. But here too it was found that the effective diffusivity over the slope was suppressed below the original scale estimate. However, instead of testing a set of empirical slope-dependent prefactors, as done by Wang and Stewart (2020) and Wei et al. (2022), this study picked up from Ferrari and Nikurashin (2010) and argued that mean flow suppression could explain the observed reduction in cross-slope fluxes near the surface, whereas eddy velocity anisotropy contributed to the reduction close to the bottom.

In other words, both sets of studies (see also Brink, 2012, 2016; Hetland, 2017) concluded that the strength of eddy fluxes over sloping bottoms is not only given by eddy energy and length (or time) scales but also by additional dynamical impacts of the bottom topography. Essentially, perfect knowledge of the eddy energy and either length scales or time scales will only produce an upper bound on eddy diffusivity. Eddy velocity anisotropy is one obvious factor which may then bring the diffusivity down from this upper bound. The other and perhaps more important factor is the possibility that velocity and tracer perturbations are not very well in phase (the two being in quadrature would give zero transport). Most likely, the topography-dependent prefactors of the above-mentioned studies primarily address such imperfect phase relationships.

The present study will focus on eddy buoyancy transport and thus on GM diffusivities. It is inspired by and builds directly on the results obtained by Wang and Stewart (2020) and Wei et al. (2022). However, as noted, the above works examined prograde and retrograde flows separately and also constructed diffusivities from eddy energy levels diagnosed from very idealized but high-resolution fields. So here we aim to i) study fluxes and diffusivities over both types of flow situations under one and the same framework, ii) examine how far one can get without diagnosing the actual eddy energy field and, finally, iii) assess the impacts both in an idealized setting and in a realistic global ocean simulation.

In the process, we also revisit the question of what is the relevant eddy length scale over continental slopes. The starting point will be the internal deformation radius since this remains a relevant parameter in the Eady problem, even when this includes a bottom slope (Blumsack & Gierasch, 1972). But we also consider the topographic Rhines scale, i.e. the scale where topographic Rossby waves (rather than planetary Rossby waves) mark the transition between linear and non-linear PV dynamics. The above-mentioned

idealized channel studies give conflicting evidence about the relevance of this scale. We are nevertheless inspired by the findings of Stammer (1997), Eden (2007) and Jansen et al. (2015) and therefore bring up this approach here again. Finally, we also examine and attempt to parameterize the role of eddy velocity anisotropy and the phase relationship between flow and buoyancy perturbations.

The paper is structured as follows: In section 2 we introduce the modelling tools and various diagnostics and parameterizations used. In section 3 we begin by diagnosing eddy fields from a high-resolution channel simulations that contain both prograde and a retrograde flows at the same time. We then see how far mixing-length and GEOMETRIC parameterizations can take us in reproducing the diagnosed depth-averaged GM diffusivity—with and without accounting for effect of anisotropy and phase relations between eddy velocity and tracer perturbations. At the end of this section we examine the impact of a topographically-aware parameterization in a coarse-resolution version of the channel model. In section 4 we finally employ the new parameterization in realistic global ocean simulation. We then take a critical look into some of our parameterization choices and their interpretation in section 5 before summarizing our findings in section 6.

2 Methods

2.1 Model setup

We use the Bergen Layered Ocean Model (BLOM), the ocean component of the Norwegian Earth System Model (NorESM; Seland et al., 2020), in an idealized channel configuration as well as in a realistic global setup. BLOM uses 51 isopycnal levels (potential density referenced to 2000 dbar) with a 2-level bulk mixed layer at the surface.

The channel setup is re-entrant in the zonal (x) direction. The domain is 416 km long (zonally) and 1024 km wide (meridionally). At both sides of the channel there are continental slopes centered at 150 km from the domain edge, stretching 2000 m in vertical from the shelf break at 250 m depth to the bottom of the slope at 2250 m depth. In addition, to trigger instabilities we add random noise with standard deviation of 10 m to the bottom topography. The model is initialized from rest with constant salinity and a horizontally homogeneous temperature profile. The temperature, which here determines density alone, has a maximum at the surface and decays exponentially towards the bottom. We place the channel in the northern hemisphere, using a constant Coriolis parameter, and then force the flow with a constant westward wind stress. The surface mixed layer is kept shallow by parameterization of submesoscale mixed layer eddies (Fox-Kemper et al., 2008) that counter the vertical mixing induced by the constant wind forcing. See Table 1 for further parameter settings.

We first run the channel model at eddy-resolving 2 km horizontal resolution. To investigate the effects of the two bottom slopes on eddy transport and, specifically, on eddy diffusivity, we vary the initial stratification and the width of the continental slope, i.e the slope angle. The various experiments are laid out in Table 2. All simulations are spun-up to a semi-equilibrium for 10 years, and the model fields are then diagnosed over an additional 5-year period (so between years 10–15). We then test and compare various forms of parameterized eddy buoyancy fluxes at coarse resolution at 32 km resolution in the same idealized channel. These are also run for 15 years, with the last 5 years being diagnosed.

Finally, the impact of the most skillful parameterization is assessed in realistic global simulations. These are nominal 1° resolution global forced ocean-ice experiments which follow the Ocean Model Intercomparison Project, OMIP-II protocol (Tsujino et al., 2020). In these simulations, the mean grid size north of 62°N and south of 64.5°S is approximately 32 km, similar to the coarse resolution channel. Two simulations are conducted,

one with the new parameterization and another with an existing eddy parameterization which does not include any effects of bottom topography. Each simulation is 110 year long (2 cycles of 55 long repeat cycle), and we diagnose the results using the last 30 years. At this point there is still a long term drift in the model (as seen in all models following the OMIP-II protocol; Tsujino et al., 2020), but the general circulation has stabilized.

2.2 Diagnostics and Paramaterizations

The key parameter of interest is the buoyancy diffusivity, as we have assumed that lateral eddy buoyancy transport can be expressed as down-gradient diffusion. In the idealized zonal channel simulations, where buoyancy is given by temperature, the cross-channel (i.e. meridional) buoyancy diffusivity can be diagnosed from

$$K_{diag} = -\frac{\langle v'T' \rangle}{\partial \langle T \rangle / \partial y}, \tag{1}$$

where v and T are meridional velocity and temperature, respectively. Angle brackets indicate a zonal (along-channel) mean and primes indicate deviations from such mean. So v' and T' are the across-channel velocity and temperature perturbations from the zonal mean.

Note that the cross-channel perturbation velocity is related to the eddy kinetic energy density

$$EKE = \frac{\langle u'^2 \rangle + \langle v'^2 \rangle}{2} \tag{2}$$

via the velocity anisotropy factor

$$A = \frac{\langle v'^2 \rangle}{\langle u'^2 \rangle + \langle v'^2 \rangle}, \tag{3}$$

so that

$$v' = (2A \cdot EKE)^{1/2}. \tag{4}$$

In practice, we use Parseval's theorem to diagnose the buoyancy flux from the cross spectrum of cross-channel velocity and temperature:

$$K_{diag} = \frac{\int \hat{C}o(v', T')\, dk}{\partial \langle T \rangle / \partial y}, \tag{5}$$

where $\hat{C}o(v', T')$ is the real part of the cross spectrum which we integrate over all zonal wavenumbers k.

In this study we focus exclusively on the depth-averaged diffusivity, and if not stated otherwise all variables are depth-averaged quantities. We leave the development of depth-varying parameterizations for future studies. A fruitful way forward for this may be to develop a flow-dependent structure function that distributes the depth-averaged diffusivity vertically (see e.g. Bachman et al., 2020; Wei & Wang, 2021). Finally, for analysis of the channel simulations, we also average K_{diag} over time.

Parameterizing the diffusivity starts with a scale estimate. Two approaches are currently in use, the traditional mixing length and the GEOMETRIC approach. In the former, we write

$$K_{ML} \propto VL, \tag{6}$$

where V is a representative eddy velocity and L is a lateral mixing scale. Typically, this is often taken to be related to the size of eddies themselves. If complete information exists about the high-resolution eddy fields, it is natural to set $V = \sqrt{EKE}$ or, more correctly for the cross-channel diffusion we study here, $V = \langle v' \rangle$. The eddy length scale

L may also be diagnosed from the shape of velocity spectra. Several possibilities exist (see e.g. Eden, 2007), but here we chose

$$L_S = \frac{\int |\hat{v}(k)|^2 k^{-1} dk}{\int |\hat{v}(k)|^2 dk} \tag{7}$$

which can be thought of as a kinetic energy-weighted mean wavelength under the spectrum.

Alternatively, the energy-based diffusivity estimate of the GEOMETRIC framework (Marshall et al., 2012; Mak et al., 2018) is constructed as

$$K_{GEOM} \propto \sigma_E^{-1} E, \tag{8}$$

where σ_E is the Eady growth rate and E is the total eddy energy. The Eady growth rate is

$$\sigma_E = 0.3 \frac{f}{Ri^{1/2}} \tag{9}$$

where f is the Coriolis parameter and Ri is the geostrophic Richardson number:

$$Ri = \frac{N^2}{|\partial U_g / \partial z|^2}. \tag{10}$$

Here

$$\begin{aligned} N^2 &= -\frac{g}{\rho_0} \frac{\partial \rho}{\partial z} \\ &= \partial b / \partial z \end{aligned} \tag{11}$$

is the squared buoyancy frequency (g is gravitational acceleration, ρ is density and b buoyancy, while ρ_0 is a reference density) and

$$\begin{aligned} |\partial U_g / \partial z| &= |\frac{g}{\rho_0 f} \nabla \rho| \\ &= |\nabla b / f| \end{aligned} \tag{12}$$

is the magnitude of the thermal wind shear. As said, E is the total eddy energy, i.e. the sum of the EKE and EPE (eddy potential energy). The latter is diagnosed from

$$EPE = \frac{1}{H} \sum_{i=1,n} \frac{1}{2} \frac{\rho_{i+1} - \rho_i}{\rho_0} g \langle \eta'^2_{i+1/2} \rangle, \tag{13}$$

where η is the height of an isopycnal surface (trivially diagnosed from the layered BLOM model). The sum is taken over n density surfaces and, as in all of the above, the prime marks deviations from the zonal mean.

Since the work on prognostic eddy energy budgets is still a topic of active research, we set out here to parameterize both the eddy velocity and eddy length scale from coarse-resolution variables. Thus, following Visbeck et al. (1997), we write

$$V_{par} = \sigma_E L, \tag{14}$$

which gives

$$K_{par} \propto \sigma_E L^2. \tag{15}$$

Two parameterizations for the eddy length scale are then assessed, namely the WKB-approximation to the internal Rossby deformation radius

$$L_R = \frac{\int N \, dz}{|f|}, \tag{16}$$

and the parameterized version of the topographic Rhines scale

$$L_T = \left(\frac{V_{par}}{\beta_T}\right)^{1/2} = \frac{\sigma_E}{\beta_T}, \tag{17}$$

where $\beta_T = (|f|/H)|\nabla H|$ and we have assumed $V_{par} = \sigma_E L_T$ (Eden & Greatbatch, 2008). Parameterized velocity and length scales are always chosen consistently i.e. the parameterized diffusivities will depend on the Eady growth rate and the squared length scale of choice.

Finally, as outlined in the introductory section, it is important to remember that the above parameterizations most likely give upper bounds on diffusivities, corresponding to situations where there is perfect correlation between the eddy velocity and temperature perturbations, i.e. where the two quantities are either in perfect phase or antiphase. To investigate if and how topographic slopes impact such phase relationship, we also utilize the high-resolution fields from the channel simulation to map out the cosine of the phase angle between the real and imaginary parts of the cross spectrum between v' and T':

$$\cos(\theta) = \frac{\hat{C}o(v,T)}{\left[\hat{C}o(v,T)^2 + \hat{Q}u(v,T)^2\right]^{1/2}} \tag{18}$$

where $\hat{Q}u(v,T)$ is the the imaginary part of the cross spectrum (the quadrature spectrum). For analysis, we average θ across all wavenumbers (k) and over time before calculating the cosine. An attempt to parameterize the observed phase relationship is also presented in what follows.

3 Eddy fluxes in a channel model

3.1 Equillibrated flow field and eddy fluxes

Our setup (see section 2.1) is very similar to the setup in the series of papers by Wang and Stewart (2018, 2020), Wei and Wang (2021) and Wei et al. (2022), except that we now have continental slopes on both sides of the channel. The forcing is also slightly different as we employ a westward wind stress which, unlike in the previous studies, is kept constant across the channel. The mean ocean state, however, is very similar. Since the channel is in the northern hemisphere, the westeard wind stress sets up a northward surface Ekman transport. Thus, Ekman divergence in the south and convergence in the north results in a time-mean sea surface tilt which is in geostrophic balance with a westward mean flow, as shown in the two upper panels of Figure 1. The Ekman-driven overturning circulation in the y-z plane lifts up isopycnals in the south so that they slope with the bathymetry there. Conversely, downwelling in the north sets up isopycnals that slope against the topography.

Despite the simple wind forcing, the total baroclinic velocity field is rather complex. In the north there is a strong westward jet over the slope. This jet has a significant thermal wind shear but nonetheless extends all the way to the bottom. Over the southern slope the westward flow is weaker and much more surface-trapped. Lower layers here are almost motionless, so the depth-averaged westward flow takes on a minimum over the slope. Instead there is a broad and nearly barotropic westward current which has its maximum strength immediately off the seaward side of the continental slope.

The north-south asymmetry is clearly not only a result of the stratification being weaker in the south than in the north. Thus, net impacts of mesoscale eddy fluxes must likely be taken into account. At the most basic level, the tilted isopycnals in both regions are baroclinically unstable, creating an eddy field whose residual mass transport will tend

to counter the Ekman-driven oveturning circulation. However, because mesoscale eddies also transport momentum, the mean flow field reflects, in part, the integrated effects of eddy momentum and buoyancy fluxes. Their combined effects can be studied in the Transformed Eulerian Mean (TEM) version of the zonally-averaged zonal momentum equation:

$$\frac{\partial \langle u \rangle}{\partial t} - f\langle v^* \rangle = -\nabla_{yz} \cdot \boldsymbol{F}_{EP} + \frac{\partial \langle \tau^x \rangle}{\partial z}, \tag{19}$$

where

$$\boldsymbol{F}_{EP} = -\langle v'u' \rangle \hat{\boldsymbol{j}} + f\frac{\langle v'b' \rangle}{N^2}\hat{\boldsymbol{k}} \tag{20}$$

is the Eliasssen-Palm flux. It consists of a lateral eddy momentum flux and an eddy form stress (this term arises after thickness-weighting). In (19) we have neglected small terms describing the transport of zonal mean momentum by the meridional mean flow as well as vertical flux of momentum (see Wang & Stewart, 2018). Note, however, that the eddy form stress term, which is connected to lateral buoyancy transport under the small-slope approximation, may be thought of as a vertical momentum flux. Finally, the Coriolis term contains the *residual* meridional velocity, i.e. the equivalent mass transport velocity which accounts for both the Eulerian-mean flow and the mass transport by eddy correlations.

The E-P flux is shown as arrows in the top panel of Figure 1. In general, both in the south and in the north, the downward eddy momentum flux is suppressed over the slopes, in agreement with earlier studies which indicate that baroclinic instability of suppressed over continental slopes. Our estimate of the depth-averaged cross-channel buoyancy diffusivity reflects this signature by being reduced by about two orders of magnitude over the continental slopes (lower panel). What these simulations show, as also seen in the simulations of Wang and Stewart (2018) and Manucharyan and Isachsen (2019), is that eddy motions instead bring zonal momentum laterally across the slopes near the surface and dump it where the ocean bottom flattens off towards the deep basin (this lateral component $< v'u' >$ is highlighted with color in the plot). And there, over the relatively flat bottom, baroclinic instability kicks in to bring the momentum down to the solid ground below.

As lateral eddy momentum fluxes are also clearly important in this and previous simulations, optimal parameterizations will likely need to be build up around down-gradient PV fluxes (see e.g. Wang & Stewart, 2018). However, it is also reasonable to expect that any framework which is successful at reproducing the order-of-magnitude drop in buoyancy diffusivities seen in Figure 1 will also improve the ocean state in coarse-grained models. So we keep this focus here. Hence, on our way towards a practical parameterization of a GM diffusivity over continental slopes, we begin by examining the length scales and velocity scales associated with the mesoscale eddy field. This approach is motivated by the mixing length argument (Prandtl, 1925), relating diffusivity to an eddy velocity scale and a length scale. However, we will also compare this approach with the energy-based GEOMETRIC framework (Marshall et al., 2012; Mak et al., 2018).

3.2 Eddy length and velocity scales

Estimates of eddy length and velocity scales are shown in Figure 2. The length scale is estimated from (7), i.e. by calculating a spectral-weighted mean wavelength associated with north-south velocity perturbations. When normalized by its mean value across the channel the length scale shows a near-universal shape across the various model runs (upper left panel). There is a broad maximum over the mid-basin before length scales drop over the continental slopes on both sides. There is, however, a consistent local maximum over mid-slope on the northern (prograde) side, coinciding with the maximum in mean zonal velocity. Scales then flatten out or even increase over the shelf regions. But, as with other diagnostics below, but we will largely ignore shelf values in the discussion below due to the proximity to the model walls. For the eddy velocity scale we show the square root of EKE. When normalized with the across-channel average (upper right panel), the

eddy velocity scale in all runs is reduced over the southern slope, save for a slight increase over the upper parts of the slope. In stark constrast, the northern slope is dominated by a large maximum, also that one centered over the upper parts of the slope. The eddy velocity then drops off and flattens out over both shelf regions.

It would seem that forming a diffusivity from the product of these diagnosed length and velocity scales may reproduce the observed reduction over the southern retrograde slope (Fig. 1), at least qualitatively. But it should also be clear that the same procedure would produce a diffusivity maximum over the northern slope—for which there is absolutely no indication in the model fields. We will return to this issue below but first examine possible scaling approximations to the observed length and velocity scales.

We start by normalizing by the classical Stone (1972) prediction. So the length scale is normalized by the internal deformation radius L_R (16) and the velocity scale by the product of the Eady growth rate (9) and the deformation radius, so $V = \sigma_E L_R$. With such normalization both the length scales and velocity scales collapse really well in the mid-basin (middle panels). The normalized length scales then drop slightly over the lower parts of both slopes, indicating that the deformation radius overestimates scales there somewhat. Finally, there is a dramatic rise in normalized scales over the upper parts of both slopes as the deformation radius drops towards the shallow shelves. As with length scales, the normalized velocities drop over the lower parts of the slopes before rising again over the upper parts. The normalization brings the EKE peak over the upper parts of the slope down to values similar to those seen over the mid-basin, suggesting that the EKE peak there coincides with the region of active baroclinic instability.

Finally, we normalize by selecting a smooth minimum of length scales:

$$L_{min} = \frac{L_R L_T}{L_R + L_T}, \tag{21}$$

where L_T is the topographic Rhines scale (17). The results are similar over the central basin since the deformation radius is the smaller of the two scales there (the Rhines scale blows up). But now both normalized length and velocity scales peak over the slopes where the Rhines scale becomes the smaller of the two—and is quite clearly too small to explain the observed fields. As such, consideration of the topographic Rhines scale does not seem to bring any improvement in skill over the continental slopes.

But before rejecting this scaling choice it is worth noting again that the construction of a diffusivity from the original (non-normalized) length and velocity scale estimates (i.e. from the curves shown in the top row) would obviously result in a diffusivity maximum over the central northern slope. Such a maximum is in no way suggested from Figure 1. What is missing from the story here is a consideration of how eddy velocity anisotropy and the velocity-temperature phase relationship may act to bring diffusivities down over the slopes. So we turn to this issue next.

3.3 Anisotropy and phase relationship

Figure 3 shows the eddy velocity anisotropy A (3) and the cosine of the phase angle between real and imaginary parts of the v' and T' cross-spectra (18). As expected, the eddy velocity field is close to being isotropic in the middle of the basin (upper panel). Values there are around 0.6, implying that cross-channel velocity fluctuations v' are in fact slightly larger than along-channel fluctuations u'. The eddy fluctuations then become much more anisotropic towards the continental slopes, with A values over the upper parts of the slope close to 0.1 (0.2) in the north (south). This implies that v' is about 70% (50%) smaller than u' in the north (south). A notable exception is a peak over the center of the northern slope where v' is about 50% larger than u'. We have also tested other measures of anisotropy, such as the velocity based measure used by K. Stewart et

al. (2015) that takes rotational aspects into account, and the results are similar to those shown here.

The general behavior of increased anisotropy over the slopes, with $|v'| < |u'|$, will work to reduce the scale-based diffusivity there. But the variations in A from mid-basin values are not great and the mid-slope peak (where $|v'| > |u'|$) would actually increase the estimates there. So we conclude from this that velocity anisotropy alone can not explain the consistent drop in diffusivity by two orders of magnitude over the slopes seen in Figure 1. The phase relation, however, is able to explain the observed order-of-magnitude drop over the slopes, as the v' and T' fields are close to 90° out of phase there (middle panel). Importantly, the low phase agreement over the northern slope largely cancels the local peak in anisotropy.

The lower panel in Figure 3 shows the product of A and $\cos(\theta)$, an indication of the total suppression of diffusivities over the scale-based upper bound. The total suppression is dominated by the information carried in the phase relationship, and velocity anisotropy primarily plays a role near the edges of the two slopes. The suppression over the slopes amounts to more than an order of magnitude, so it is an effect which clearly needs to be parameterized.

Essentially, the slope-dependent prefactors which previous studies have needed to invoke to explain buoyancy diffusion in similar channel simulations are attempts at such parameterization (Brink, 2012, 2016; Hetland, 2017; Wang & Stewart, 2020; Wei et al., 2022). However, at this point we temporarily detour from those earlier studies and instead take as a starting point an expression which bears some resemblance to the final form of the mean flow suppression expression proposed by Ferrari and Nikurashin (2010). Thus, we construct an eddy efficiency factor as

$$E_{eff} = a_1 \frac{1}{1 + a_2 \left(U_{bc}^2 / V^2\right)}. \tag{22}$$

Here, U_{bc} is the large-scale baroclinic flow speed obtained after subtracting the depth-averaged velocity, V is the eddy velocity scale and a_1 and a_2 are scaling factors which we here take to be constant. The expression does not have a rigorous basis but a simple intuitive interpretation. U_{bc} is directly related to the thermal wind shear and, hence, to the underlying energy source of baroclinic instability (e.g. Sutyrin et al., 2021). Qualitatively, if U_{bc} is large and the flow is baroclinically unstable, one would expect V to be relatively large, giving $E_{eff} \sim 1$. But if V remains small despite large U_{bc}, some dynamical constraints (e.g. a sloping bottom) must be reducing the efficiency of baroclinic energy conversion, implying $E_{eff} \ll 1$.

We evaluate (22) at each depth but then take the mean over the water column. The large scale baroclinic flow U_{bc} is extracted directly from the resolved (and zonally-averaged) velocity field, while the eddy velocity is parameterized from (14). The lower panel of Figure 3 shows the resulting efficiency factor, using either L_R or L_T as length scale. The tuning constants a_1 and a_2 have been chosen manually but it is clear that using $L = L_T$ can produce a suppression over the continental slope which is in fairly good agreement with $A{\cdot}\cos(\theta)$ over both slopes for a range of different simulations. We note that several tests with using the thermal wind instead of U_{bc} and with evaluating (22) with depth averaged-quantities (instead of taking the mean of a depth dependent expression) all produce similar results. Here we chose to use U_{bc} due the ease of implementation at coarse resolution.

3.4 Parameterized diffusivity

Given the above results, we then proceed with parameterizing the diagnosed buoyancy diffusivity. The aim is to capture the order-of-magnitude reduction in diffusivities from the mid-basin to the slope regions. The results are shown in Figure 6 where we dis-

tinguish between diagnostic (panels a–c) and full parameterizations (panels d–e). The diagnostic parameterizations include information about the mesoscale field itself which would not be directly available in a coarse resolution model (but could be parameterized in higher-order schemes), whereas the full parameterizations use large-scale metrics only and are therefore suitable for direct implementation in any existing coarse-resolution model. Panels a and c are from one single simulation, showing both the actual depth-averaged diffusivity diagnosed (black line) and the various approximations (distinguished by Roman numerals and color). Panels b–c and e–f then show statistics over both slope regions collected over the whole range of simulations.

A first thing to notice from the diagnostic parameterizations (panels a–c) is that the mixing length (I) and GEOMETRIC (II) approaches behave very similarly. As also noted by Wang and Stewart (2020), both give reduced diffusivities over the southern retrograde slope and produce a reasonable fit there ($r^2 > 0.6$). But the reduction is still underestimated by up to one order of magnitude. In the north, over the prograde slope, both approaches result in a serious qualitative mismatch as the high EKE levels there (seen in Fig. 2) produce a non-existing diffusivity peak over mid-slope.

The observed discrepancies, particularly the qualitative mismatch over the northern slope, confirms that scaling arguments alone are unable to create diffusivities that reproduce the observed buoyancy transport across the slope regions. Accounting for the diagnosed eddy velocity anisotropy, so that $\sqrt{EKE}$ will be replaced with v' (III) improves the mixing length estimate slightly but not nearly enough. Multiplying the two estimates by $A\cos\theta$, however, largely removes the diffusivity peak in the north and even produces a clear suppression over the slope (IV and V). The values are still higher than the observed diffusivity, but the regression slope is close to one and the correlation r^2 values above 0.8. Over the retrograde slope in the south the match is even higher.

Guided by the observed agreement between the mixing length and GEOMETRIC estimates above, we focus on the former approach when examining how well full paramaterizations can do. So we assume that a diffusivity can be written as the Eady growth rate times the square of a length scale. Including our efficiency factor, the effective diffusivity becomes

$$K = a_1 \frac{K_0}{1 + a_2 \left(U_{bc}^2 / V^2\right)}, \tag{23}$$

where $K_0 = \sigma_E L^2$ is the scaling estimate of diffusivity before considering the efficiency factor and where, as discussed above, we have a choice to make for the length scale. We start by looking at K_0 first. Using the traditional Stone (1972) expression where the length scale is taken to be the internal deformation radius everywhere, seriously overestimates diffusivities over both slope regions (VI). The estimate, in fact, bears some resemblance with both the mixing length and GEOMETRIC estimates based on diagnosed eddy quantities (I and II), but with even larger discrepancies over the slope regions.

Selecting as length scale the smooth minimum of the deformation radius and the parameterized topographic Rhines scale (VII) improves the estimate dramatically. The results are unchanged over the flat regions, as the deformation radius is selected there. But over the slopes where the Rhines scale is selected, the parameterized diffusivities drop by up to two orders of magnitude and start to match the observations quite well (with $r^2 > 0.8$ over both slopes). Multiplying this estimate with the parameterized efficiency factor (VIII) improves the match somewhat over the prograde slope in the north but not, as it turns out, over the retrograde southern slope.

Both Figures 3 and 6 indicate that Stone scaling, i.e. using the deformation radius as length scale, produces better estimates of observed eddy characteristics than does the topographic Rhines scale. And yet, these simulations suggest that applying the Rhines scale is absolutely crucial in reproducing the observed diffusivity reduction over topographic slopes. This apparent contradiction may suggest that our parameterized topo-

graphic Rhines scale does not reflect the physical size of equilibrated eddies but rather a reduction in the effective mixing length. In other words, the mixing length is not trivially related to the eddy size. Given our parameterization, the effect will impact the scaling estimate significantly so that the need for an explicit suppression factor (our E_{eff}) becomes smaller. But we leave further speculation on this topic to the discussion section and here carry on to see what effects the parameterized expression (VIII) will have in actual coarse-grained simulations.

3.5 Performance in a coarse-resolution channel simulation

The coarse-resolution channel setup is similar to the high-resolution channel setup, except for resolution (from 2 km to 32 km) and the activation of the GM-Redi parameterization scheme. The model is forced and run similarly to the high-resolution setup. Figure 5 shows parameterized buoyancy diffusivities and the top-to-bottom thermal wind shear from three of the equillibrated simulations that had wide continental slopes but differing initial stratification. We also show the corresponding diagnosed quantities from the corresponding high-resolution simulations for comparison (thick black lines), but it should be remembered that that one is a distinct simulation. As in Figure 6, we show the three versions of the parameterized diffusivity (and corresponding thermal wind shears): one using the internal deformation scale (with $a_1 = 8$), one using the smooth minimum between internal deformation scale and topographic Rhines scale (with $a_1 = 8$) and, finally, one using the smooth minimum and also applying the parameterized eddy efficiency factor (with $a_1 = 32$ and $a_2 = 1$). In the last case a_1 is tuned so that the parameterized buoyancy diffusivity matches the two former cases in the mid-basin.

The results show that over the mid-basin, where the internal Rossby radius will always be selected as length scale, the parameterized diffusivity magnitude corresponds fairly well to the diagnosed diffusivity in the mid-basin. However, the parameterized diffusivity shows a clear north-south gradient in the magnitude, an effect caused by a stronger difference in stratification between north and south at coarse resolution which directly impacts the internal deformation radius. The deformation scale-based parameterization (orange line) then suggests local diffusivity maxima over both slopes, as also seen in Figure 6. This run has a thermal wind shear which is not at all enhanced over the continental slopes. Essentially, the high eddy buoyancy transport over the slope regions effectively washes out any density front there. This, it should be remembered, is exactly the effect one wishes to reduce with a slope-sensitive parameterization.

The run using a parameterization which selects the minimum of the two length scales does much better over both continental slopes where the topographic Rhines scale kicks in. With suppressed diffusivities, the density front which is set up by the topographic PV gradient is no longer washed out completely. The result is an enhanced thermal wind shear over the northern slope, albeit with a lower absolute strength than in the high-resolution simulation. In the south, where the stratification is much weaker, the parameterization is not able to set up a thermal wind shear.

Further scaling by the eddy efficiency E_{eff} (Fig. 5, green) enhances the diffusivity reduction in the north, but not necessarily in the south, as also observed for the high-diagnostics simulations. Therefore, the feedback to the resolved fields strengthens the baroclinic jet in the north further, but not in the south.

The above results are encouraging. However, although the channel setup is a reasonable test bed for development, it is extremely idealized and lacks multiple features from the real world (e.g. variable Coriolis parameter, uneven topography and complex atmospheric forcing). Therefore, we also test the slope-aware parameterization in the realistic global domain next.

4 Realistic global model simulations

4.1 Eddy parameterization adjustments

We carry out a 'control' simulation and 5 different perturbation experiments, but for simplicity, we focus on a comparison between the 'control' simulation and two of the perturbation experiments. All of these simulations operate with 2D diffusivities based on the depth-averaged Eady growth rate and a square length scale, as in (15). The control run selects a length scale from the minimum of the internal deformation radius and the planetary Rhines scale. Then, in two distinct 'topo' runs we i) introduce the topographic Rhines scale in the minimum function and ii) also turn on the eddy efficiency factor E_{eff}. The OMIP 'topo' runs then differ slightly from the coarse-resolution channel setup in the choice of constant scaling factors. The constant factor a_1 which scales the overall diffusivity magnitude is set to 3 and factor a_2 used in E_{eff} is set to 1. In addition, we scale the topographic Rhines scale further down with a constant factor 0.5 (stronger sensitivity to slopes). We view these constants as tuning factors specific to one particular setup; for example, the resolution of the bottom topography dataset influences the strength of the topographic beta and thereby tuning the topographic Rhines scale might be needed. Finally, in all runs the diffusivity magnitude is scaled down with a resolution function (Hallberg, 2013) when the deformation radius is resolved by the model grid. And, for simplicity, the along-isopycnal (Redi) tracer diffusivity is set to be the same as the GM diffusivity.

To put these experiments in some context, it should be mentioned that the model settings for the control run are similar to the NorESM model version used in the latest Climate Model Intercomparison Project (CMIP6) except for the GM diffusivity formulation. The CMIP6 version of the model included a mixing length formulation where the length scale was selected as the minimum of the internal deformation radius and the planetary Rhines scale—as in our control simulation. However, the local Eady growth rate was then evaluated at each model level, rendering a 3D profile for both eddy driven advection (GM) and for along isopycnal mixing (Redi). Finally, the scaling-based diffusivity was adjusted by a zonal velocity-dependent mean flow suppression following Ferrari and Nikurashin (2010), and as in the experiments here, a resolution function (Hallberg, 2013) was also used.

The lack of vertical structure of the 2D parameterization proposed here, turned out to be a clear deficiency in the global domain as our initial simulations showed an unrealistically strong sensitivity to bottom slopes in the low and mid-latitude deep ocean. For example, large reductions in the parameterized diffusivity across mid-ocean ridges were not seen in eddy-permitting studies that diagnosed eddy diffusivity in the global domain (e.g., Bachman et al., 2020). Therefore, to reduce the topographic impact on eddy fluxes in strongly stratified low and mid-latitude regions, we added an ad hoc 'limiter' of topographic effects—based on the assumption that if the resolved flow does not feel the bottom then it is unlikely that mesoscale eddies would do so either. Specifically, the topographic Rhines scale is scaled by $\cos(\alpha)^{-10}$ which rapidly increases the topographic Rhines scale when the angle α between the resolved flow and the bottom slope tangent vector deviate by more than $\sim 30^\circ$ i.e. when the resolved flow is not aligned with the bottom slope.

4.2 Model response in the global domain

As expected, introducing the topographic Rhines scale leads to locally reduced diffusivities over sloping topography, as shown in Figure 6 (top row). The effect is enhanced at high latitudes with a $\sim$50% reduction over Arctic and Antarctic continental slopes. Bringing in the eddy efficiency E_{eff} leads to additional and more severe diffusivity reduction globally, also away from topographic features (bottom row). This is in agreement with other recent studies that found the scaling by mean-flow dependent suppres-

sion to have the largest impact on diffusivity at global scale (Stanley et al., 2020; Zhang & Wolfe, 2022; Holmes et al., 2022). Note that in the tropics, the diffusivity is limited by the grid resolution function (Hallberg, 2013), i.e. the diffusivity is reduced when the grid size is smaller than the local deformation radius. Therefore, the large relative reduction in tropical diffusivity is small in absolute terms and less important there as transport is dominated by the resolved flow. Finally, we note that a comparison between the top and the bottom rows in Figure 6 shows that in multiple continental slope regions, especially in the Arctic and around Antarctica, the eddy efficiency simply enhances the response seen with the topographic Rhine scale but the pattern stays the same. Indeed, the diffusivity reduction due to introducing the topographic Rhines scale and due to eddy efficiency are close to linearly additive (not shown).

As the impact of eddy efficiency on diffusivity is more broad, its impact on flow speed, temperature, and salinity is also more widespread than the impact of the topographic Rhines scale alone. Table 3 collects bias reductions (relative to the control case) across 5 different experiments while Figures 7–9 show the spatial patterns for subsurface (100–200 m) current speed and temperature, as well as zonal-mean temperature and overturning anomalies for the two 'topo' experiments that are in focus here. We show results for the subsurface response since the surface response in these forced simulations is strongly forced by the non-responsive atmosphere. Both the topographic Rhines scale alone and its combination with eddy efficiency increase the mean kinetic energy of the resolved flow globally (at 100–200 m depth, by 2.7% and 10.5%, respectively). This increase is especially noticable over sloping bathymetry where the two impacts contribute approximately equally to the overall increase (100–200 m depth where $\beta_t > 5E{-}10$ m^{-1}s^{-1}, by 9.1% and 20.8%, respectively). The two modifications also warm the ocean below the global thermocline and cool the surface, reducing the overall temperature bias at depth. But they increase the temperature bias at the thermocline (Table 3; Fig. 9a,c). Overall, the mean overturning response in the 'topo' runs is characterized by a positive (cyclonic) anomaly which implies that the Atlantic overturning cell and the Deacon cell in the Southern Ocean strengthen, whereas the Antarctic Bottom Water cell and the shallow surface overturning cells within the subtropical and subpolar gyres weaken. These changes generally reduce biases. The simulated strength of the Atlantic overturning at $26°N$ is 15.5 Sv in the the control simulation, 17 Sv when topographic Rhines scale is considered, and 18 Sv with the addition of eddy efficiency, whereas the observational estimate from the RAPID array ($\sim$26°N) is 17$\pm$3.3 Sv (Frajka-Williams et al., 2019). The Antarctic bottom water cell at 32°S weakens from 26.0 Sv in the control simulation to 23.5 Sv with topographic Rhines scale and 20.3 Sv with addition of eddy efficiency, whereas inverse modelling suggest 20.9$\pm$6.7 Sv (Lumpkin & Speer, 2007). The Deacon cell strengthens from 13.2 Sv in the control simulations to 15.2 Sv with the topographic Rhines scale and 18.4 Sv when eddy efficiency is considered, whereas previous modelling estimates (Döös et al., 2008) and observational estimates (Speer et al., 2000) suggest a strength of 20 Sv and 20-25 Sv, respectively. The vertically-integrated mass and heat transports, plotted in Figure 10, show that overall the overturning response leads to increasing heat transport towards the northern hemisphere. The northern hemisphere subtropical peak in northward heat transport in the Atlantic basin (globally) is 0.83 PW (1.07 PW) in the control simulation, 0.91 PW (1.15 PW) when topographic Rhines scale is considered, and 1.00 PW (1.26 PW) with the addition of eddy efficiency, whereas Trenberth et al. (2019) estimate approximately 1.1 PW (1.6 PW).

Some more specific impacts of the topographic Rhines scale and eddy efficiency are a poleward shift and strengthening of the boundary and slope currents, with E_{eff} generally speeding up the boundary currents at locations where observations show the core of the currents (Fig. 7, observed currents in black). Changes in the net volume transports in most key passages remain small (Table 4), but the results show a strengthening of the ACC (Drake Passage transport; increased bias), a general enhancement of water exchange between the Arctic and mid-latitudes (opposing influence on the bias in dif-

ferent straits), and strengthening of the Gulf Stream (Florida–Bahamas strait transport, reduced bias). The spinup of the ACC is a direct consequence of reduced diffusivities, allowing for stronger thermal wind currents. In the northern North Atlantic, the current speed response is directly reflected in the temperature response as the Atlantic Water warms up along its path from the Nordic Seas to the Arctic (Fig. 8, reduced bias). Despite the speed-up of the Gulf Stream off the North American coast, its observed turning around Grand Banks off Newfoundland is not reproduced. Due to this deficiency, the cold bias off Newfoundland strengthens (Fig. 8). This cold bias is a long standing issue in coarse resolution ocean models (Tsujino et al., 2020) and reducing the diffusivity along the current path or along the shelf break clearly does not mitigate the bias. We speculate that, similar to the southern retrograde slope in the channel configuration and recent results on the Gulf Stream reported by Uchida et al. (2022), the eddy momentum flux convergence that is not included in the parameterization plays a crucial role in determining the current path.

Figure 10 summarizes the zonally-integrated impacts, breaking both volume and heat transport into resolved and parameterized eddy components. It illustrates how the reduced eddy mass transport across the ACC (panels a–b) also leads to less poleward heat transport (panels c–e) and therefore a cooling of the Southern Ocean surface, but also warming over the continental slopes (Fig. 8). Both these effects reduce the bias in the model. Note that the heat transport response is dominated by eddy-driven advection with a smaller contribution due to the eddy diffusion (panels d–e). In contrast to the Southern Ocean, in the northern mid-latitudes the overall northward mass and heat transport increase as the mean overturning spins up (Fig. 10 panels a and c; Fig. 9 right panels) and the eddy contributions actually weaken (Fig. 10, panels b, d–e).

We note that since both the eddy efficiency and the topographic Rhines scale act to reduce the diffusivity, there is a limit to the effectiveness of these parameterizations because other processes and, specifically, the resolved flow start to dominate the model solution as the diffusivity weakens. For example, the reduction of globally integrated temperature and salinity biases seem to saturate as the topographic Rhines scale is tuned down and the eddy efficiency scaling is included (Table 3). This highlights the need to test parameterizations in realistic global settings and cautions against drawing conclusions of the effectiveness and utility of a parameterization based on assessing the diffusivity magnitude alone.

5 Discussion

Our study has focused on a relatively small range of parameterization choices, essentially i) re-examining the topographic Rhines scale as a relevant mixing length and ii) checking the importance of an additional suppression factor which we have called the eddy efficiency E_{eff}. The quite similar idealized studies by Wang and Stewart (2020) and Wei et al. (2022) did a more comprehensive sweep over possible parameterization choices but did not analyse prograde and retrograde bottom slopes under one and the same framework, which has been the intention here. Also, to the best of our knowledge, the current OMIP simulations constitute the first assessment of the impacts of a topographically-aware GM parameterization in realistic global ocean models. As such, this work should be taken as a pragmatic investigation into what can be achieved with simple parameterization approaches applied to existing models that do not contain a prognostic eddy energy equation (which in itself requires parameterization choices). As with all parameterizations, the options examined here are far from perfect, and below we discuss some shortcomings and unresolved questions.

5.1 The relevance of the topographic Rhines scale

Earlier idealized model studies have given conflicting evidence for the relevance of the topographic Rhines scale. Jansen et al. (2019) reported that a using a generalized Rhines scale which accounts for both planetary and topographic beta in their eddy parameterization of flows in an idealized ACC-like domain improved their model skill. But the study, whose primary focus was on parameterizing an eddy energy budget, did not examine the length scale issue at any depth. More in line with our work here, the idealized channel studies of Wang and Stewart (2020) and Wei et al. (2022) found the topographic Rhines scale to be a useful choice over retrograde slopes—but not over prograde slopes. This conclusion was drawn, however, after an empirical slope-dependent prefactor was applied in the retrograde case but not in the prograde case. Both studies also constructed diffusivities from diagnosed depth-averaged EKE. In other words, they set the eddy velocity scale to be $V = \sqrt{EKE}$ and then defined $L_{Rh} = \sqrt{V/\beta_t}$, i.e. using the actual definition of the topographic Rhines scale. Our Figure 2, however, shows an EKE peak over the prograde slope which, if using their definition would clearly overestimate diffusivities over this slope. Here we find, somewhat surprisingly, that a full parameterization, using the Eady growth rate and the topographic beta parameter, produces a suppression over both prograde and retrograde slopes which nearly matches the 'observations' diagnosed from our high-resolution channel model.

We do not have a good understanding of this apparent paradox. But one possible problem with constructing a topographic Rhines scale from depth-averaged EKE is the fact that in a baroclinic system it is the bottom eddy velocity, rather than the depth-average, which should enter into the formulation. No considerations of the vertical structure of the eddy velocity was made here, but we suggest that future work on the topic investigates the skill in an equivalent barotropic formulation of the eddy velocity.

Moreover, the results shown in Figure 6 suggest that much of the discrepancy between the pure scaling-based diffusivity and the actual diffusivity is contained in the suppression factor which ours and other studies have pointed to. Essentially, the imperfect phase relationship between eddy velocity and buoyancy perturbations reduces the efficiency of eddy transfer by up to two orders of magnitude over continental slopes, possibly with larger suppression over prograde conditions. Any skilfull parameterization clearly needs to try to account for this effect.

5.2 The interpretation of E_{eff}

Our parameterized expression (22), which is able to qualitatively reproduce such suppression, looks superficially similar to the final form of the mean-flow suppression expression of Ferrari and Nikurashin (2010, their equation 17). This first seems odd, given that their findings have traditionally been applied to tracer (Redi) diffusion and, as mentioned in the introduction, appears to quite successfully explain a reduction in passive tracer diffusion over a retrograde continental slope in the idealized simulations of Wei and Wang (2021). But eddy buoyancy transport at any one depth in the ocean is advective rather than diffusive, so it's not at all obvious that the kinematic arguments of Ferrari and Nikurashin (2010) should apply to buoyancy diffusivities.

Indeed, Abernathey et al. (2013) use high-resolution model simulations to show that the vertical structure of buoyancy diffusivities differs from that other tracer diffusivities (including PV diffusivities). And yet, as their equation 24 suggests, the depth-averaged value of the buoyancy diffusivity should be similar to that of PV and passive tracer diffusivities, at least in the case where the planetary vorticity gradient can be neglected. This makes some intuitive sense since one end result of a depth-integral of an eddy-induced overturning circulation, driven by baroclinic instability and with zero top-to-bottom volume transport, is a 'diffusive' buoyancy transport down the lateral buoyancy gradient (the other end result is an up-gradient vertical buoyancy transport).

But there are still difficulties with equating our E_{eff} with the mean-flow suppression formulation of Ferrari and Nikurashin (2010). Their suppression effect builds fundamentally on the propagation speed of eddies relative to that of the mean flow. It is based on a set of key key assumptions, including the dominance of one wavenumber and a relationship between eddy decorrelation timescale, wavenumber and EKE. And in reaching their final equation 17, which takes on a form similar to our (23), they make the further assumption that the eddy speed is proportional to the mean flow speed. Since Ferrari and Nikurashin (2010) originally studied suppression at the sea surface, using satellite altimeter observations to pin down both mean and eddy velocity scales, this amounted to having to tune one proportionality constant. How their final expression 17 can be applied through out the entire water column, as we're aiming for here, is less obvious. So we leave a further investigation into this particular relationship for future work.

It should also be mentioned that our E_{eff} can be related to the slope-dependent prefactors of some of the earlier channel studies as well as to a controlling parameter in the topographic Eady problem of Blumsack and Gierasch (1972). This connection becomes apparent if we evaluate the 2D version of (22). We begin by setting $U_{bc} = U_{tw}$, where U_{tw} is the top-to-bottom thermal wind shear (a 2D quantity). Then we first consider the slope region where the topographic Rhines scale will be the relevant length scale. So, here, $V = \sigma_E^2/\beta_T$, where σ_E is now the depth-averaged (2D) Eady growth rate. Noting that in the Eady model, where both N^2 and $\partial U_g/\partial z$ are constant, $\sigma_E = 0.3 \cdot U_{tw}/L_R$. This allows us to rewrite (22) as

$$\begin{aligned} E_{eff} &= a_1 \frac{1}{1 + a_3 \left(\beta_T L_R^2/U_{tw}\right)^2} \\ &= a_1 \frac{1}{1 + a_3 \delta^2}, \end{aligned} \tag{24}$$

where a_3 is a modified tuning factor. Here $\delta = \beta_T L_R^2/U_{tw}$ is the slope parameter of Blumsack and Gierasch (1972) which measures the ratio between topographic and isopycnal slopes.

This expression is interesting not only because it brings in the controlling parameter of the modified Eady problem but also for its similarity to the slope-dependent prefactor used by Wang and Stewart (2020) over retrograde slopes in the parameter regime where the bottom slope is not much larger than the isopycnal slope. Their prefactor F_{MLT} (from their table 3) has the topographic delta parameter to the power of one in the denominator, in contrast to our squared power. But we suggest that the impact of sampling errors in the empirical fitting be studied in future studies before the correspondence is rejected. We also note that the similar studies of prograde fronts by Brink (2016) and Wei et al. (2022) found best fits using similar expressions but using topographic Burger number Bu in place of the delta parameter, where the two are related via $Bu = (\sigma_E/f)\,\delta$. The latter study concluded that scalings using δ instead of Bu where not successful over prograde slopes. But, again, a comparison with our results are not straightforward since their diffusivities were constructed using diagnosed EKE while ours were fully parameterized. The relationship between δ-based and Bu-based formulations is an obvious topic for future work.

Note, finally, that over the flat regions where the deformation radius will act as the relevant length scale, the 2D version of our efficiency factor becomes constant, in agreement with the behavior seen in Figure 3. In fact, the 2D version of E_{eff} was able to qualitatively reproduce the observed eddy efficiency behaviour in the idealized channel simulations, with some changes required for the tuning constants (not shown). We nonetheless chose to use the 3D version in the realistic OMIP simulations in anticipation of a more complex hydrography and flow field where the various assumptions of the Eady model can be expected to hold to an even lesser degree than in the channel model. Interior thickness PV gradients, for example, are expected to be small in systems that are only forced by Ekman pumping, as our channel model is (see e.g. Meneghello et al., 2021; Manucharyan

& Stewart, 2022). In a real ocean, where e.g. thermohaline forcing can produce interior PV gradients, the suppression of eddy efficiency will inevitably be governed by additional non-dimennsional parameters beyond Blumsack and Gierasch (1972) δ (or, alternatively, the topographic Burger number). Such 3D effects, caused by thermohaline forcing in addition to wind stress, may also be the underlying reason for why E_{eff} had a much bigger impact in the OMIP simulations than it did in the channel.

6 Summary and conclusions

Efforts to include topographic effects into mesoscale eddy parameterizations are warranted, especially at high latitudes where observations show that hydrographic fronts are typically locked to topography. The very existence of such fronts along continental slopes and submarine ridges imply not merely topographic steering of large-scale currents but also suppression of mesoscale stirring across topography. Yet, despite all the observational evidence, as well as solid theoretical arguments for e.g. reduced growth rates and length scales of baroclinic instability over sloping topography, most eddy parameterizations still fail to account for any bathymetric influence.

Here we have re-examined the relevance of the topographic Rhines scale in the mixing length approach to parameterizing the Gent-McWilliams diffusivity which is used for eddy advection. Constructing diffusivities using the Eady growth rate and a parameterized version of the topographic Rhines scale reproduces an observed order-of-magnitude reduction in diffusivity over continental slopes in idealized channel simulations. The simulations and analysis cover both prograde and retrograde continental slopes, representing mean flows in the same and opposite direction to topographic waves, respectively. Although differing in detail, both the observed and parameterized stirring suppression are of similar order of magnitude on both sides. The skill of the parameterization is enhanced further, at least over the prograde slope, when the diffusivity is multiplied by an eddy efficiency factor E_{eff} that is sensitive to the strength of the mean flow vertical shear relative to the parameterized eddy velocity scale. Finally, we find that selecting a smooth minimum of the topographic Rhines scale and the internal deformation radius for length scale gives good skill over the entire idealized channel domain.

The parameterization is then tested in a realistic global ocean simulation. Comparison with a simulation where topographic effects on the GM diffusivity are not included suggests that the parameterized topographic stirring suppression enhances the sharpness of hydrographic fronts and, as such, strengthens the thermal wind shear in boundary currents. The improvement is particularly noticeable at high latitudes, but we also observe large impacts throughout the world oceans. The globally-integrated temperature and salinity bias reductions range from O(1%)-O(10%), with largest reductions seen in Southern Ocean temperatures and in Atlantic Water temperatures in the Arctic. However, existing low-latitude thermocline biases tend to increase. This is not uncommon in a complex model as global bias reduction is very much a tuning exercise involving a range of free parameters associated with different parameterizations (e.g. eddy transport, vertical mixing and air-sea-ice fluxes). Our parameterization also has free parameters and, as is common, we found that the different model configurations might need different values for these. But we did not attempt a rigorous tuning, especially not for the dynamically complex OMIP simulations. Our focus at this stage has not been on a well-tuned realistic global simulation, but rather on illustrating possible impacts of a topography-aware eddy parameterization.

The suggested parameterization is clearly incomplete. The large difference in importance of the efficiency factor E_{eff} between the channel simulations and the realistic OMIP simulations is one indication of this. A second one is the fact that we had to use an ad hoc limiter when applying this in the OMIP simulations. One key problem is likely that we have been ignoring any vertical structure in eddy velocities and, ultimately,

diffusivities. Fundamentally, the kinematic interaction with the bottom involves eddy bottom velocities, and a number of observations as well as theoretical arguments have indicated that these are often significantly smaller than surface or even depth-averaged eddy velocities (see e.g. Killworth, 1992; Wunsch, 1997; de La Lama et al., 2016; Lacasce, 2017). The topographic impact, under such considerations, would probably be smaller than if estimated with depth-averaged quantities. Future work clearly needs to be put on such vertical structure, for example by taking an equivalent barotropic structure as a starting point (Killworth, 1992). We also observe that in our coarse-resolution channel simulations the flow remains too baroclinic, similar to the results by Kjellsson and Zanna (2017); Yankovsky et al. (2022). Although addition of vertical structure to the buoyancy diffusivity might mitigate the issue, feeding the mean flow with vertically distributed eddy energy might be needed to resolve it (Yankovsky et al., 2022).

A related issue which we have entirely neglected in this study is the impact of bottom roughness or corrugations on fluxes—and how such impact may be asymmetric with respect to the flow direction. As demonstrated by Wang and Stewart (2020), bottom roughness along a retrograde topographic slope can set up additional eddy buoyancy transport and, thus, form stresses due to arrested topographic waves. The dynamics governing such fluxes are likely distinct from those captured by our parameterizations here for smooth topography. The relevant eddy length scale, for example, is probably not the the same as for transient eddies, as indicated in the study by Khani et al. (2019) of transient vs. standing contributions to eddy form stress in an idealized Southern Ocean domain. The application of standing Rossby wave theory (e.g. Abernathey & Cessi, 2014; A. L. Stewart et al., 2023) appears to give promising results on the planetary beta plane with a flat but rough bottom. A natural next step may therefore be to examine such ideas to the 'topographic beta' problem, using e.g. the idealized two-slope model used here.

Yet another issue ignored here is the role of lateral eddy momentum fluxes over continental slopes. As shown in Figure 1 and also highlighted in earlier studies (e.g. Wang & Stewart, 2018; Manucharyan & Isachsen, 2019), such fluxes bring wind momentum off the slopes to relatively flat regions where baroclinic instability kicks in to transfer the momentum to the ground below. The lateral momentum flux may be up-gradient in places and form eddy-driven jets, as seen offshore of the retrograde slope in our idealized simulations (Fig. 1). And, as for eddy form stress, lateral momentum fluxes also appear to be impacted by corrugated bottoms, being associated with the formation of prograde jets near the bottom (Wang & Stewart, 2020). This last effect is again probably related to the formation of arrested topographic waves, as discussed by (e.g. Haidvogel & Brink, 1986), as well as being linked to down-gradient PV diffusion in the finite-amplitude limit Bretherton and Haidvogel (1976); Vallis and Maltrud (1993).

Finally, it's worth remembering that eddy diffusion, even of buoyancy, may be anisotropic. So what really needs to be parameterized is a diffusion tensor rather than a single scalar. Bachman et al. (2020) discussed such anisotropy of the diffusion tensor and showed that at global scale the direction of the major axis of the tensor is well correlated with the mean flow direction and the minor axis is well correlated with the gradient of Ertel PV. In addition, Nummelin et al. (2021, Appendix A) suggested that in terms of Redi mixing, the Ferrari and Nikurashin (2010) type of mean flow suppression indeed suppresses the across-flow mixing, but that the inverse of the same factor enhances mixing in the along-flow direction. It remains unclear whether our eddy efficiency factor and the other empirical scaling factors (e.g. Wang & Stewart, 2020; Wei et al., 2022) act similarly (i.e. relate to tensor anisotropy) or if they indeed suppress the overall tensor magnitude. In other words, it remains a research question whether the mean flow and topography merely direct the eddy transport or if they impact the overall magnitude of the eddy transport. Nevertheless, if the tensor major axis is correlated with the mean flow (as suggested by Bachman et al., 2020) —and if that mean flow transport dominates over eddy transport— then the focus on the minor axis is likely justified.

Table 1. BLOM model constants for the channel simulations

Name	Symbol	Value
Wind stress	τ_x	0.05 N m^{-2}
Horiz. grid size	Δx, Δy	2 km
Baroclinic timestep	Δt	120 s
Domain x-size	L_x	416 km
Domain y-size	L_y	1024 km
Gravitational acceleration	g	9.806 m s^{-2}
Coriolis parameter	f_0	1×10^{-4} s^{-1}
Slope mid-point distance from domain edge	Y_S	150 km
Shelf depth	H_{Shelf}	250 m
Slope height	H_{Slope}	2000 m

Table 2. Channel model experiments. L_{Rossby} is the mean deformation radius in the central basin (where bottom depth is larger than 2250 m).

Name	L_{Rossby}	Slope Width
Exp 1	34.1 ±1.3 km	75 km
Exp 2	34.1 ±1.1 km	100 km
Exp 3	34.4 ±1.0 km	125 km
Exp 4	30.6 ±1.3 km	75 km
Exp 5	30.6 ±1.2 km	100 km
Exp 6	30.4 ±1.0 km	125 km
Exp 8	24.9 ±1.2 km	75 km
Exp 9	25.9 ±1.0 km	100 km
Exp 10	24.9 ±1.0 km	125 km

So important questions remain. But despite its many shortcomings, the relatively simple parameterization investigated here at least reduces an excessive washing out of hydrographic fronts over submarine ridges and continental slopes in ocean climate models—a known problem with eddy parameterizations that are insensitive of bathymetry. One of several important consequences of such adjustment is likely a more accurate representation of oceanic heat transport across Antarctic and Greenland continental slopes and onward to the great ice sheets whose melt rates depend intimately on such transport. For this and other reasons, further scrutiny of all of the above unresolved issues and their impacts in both regional and global realistic simulations are much needed.

7 Open Research

The model configuration is available at https://github.com/NorESMhub/BLOM and the specific namelist for running the experiments used in this study can be obtained from the first author. The key model output and scripts to reproduce the data are made available through https://archive.norstore.no/ and will be made available through https://github.com/AleksiNummeli upon publication.

Table 3. CORE-II hydrography bias (root mean square error) reduction compared to the bias of the control case. The observational data sets are the WOA 2018 climatologies for temperature (Locarnini et al., 2018) and salinity (Zweng et al., 2018).

Name	zonal mean T	zonal mean S	$T_{100-200m}$	$T_{200-500m}$	$T_{500-1000m}$
L_T	6%	4%	-2%	1%	3%
$0.5 \cdot L_T$	12%	9%	-4%	3%	7%
E_{eff}	25%	21%	-11%	2%	12%
L_T and E_{eff}	28%	24%	-13%	2%	16%
$0.5 \cdot L_T$ and E_{eff}	28%	26%	-16%	2%	18%

Table 4. Observed and simulated current transport in selected straits. The various perturbation experiments show percentage changes relative to the control case. The references for the observational values are as follows: Arctic Ocean gateway transports come from de Boer et al. (2018) with the original citations being Ingvaldsen et al. (2004) for Barents Sea Opening, Beszczynska-Möller et al. (2015) for Fram Strait, Curry et al. (2014) for Davis Strait (CAA), and Woodgate (2018); Woodgate et al. (2015) for Bering Strait; ACC transport come from Xu et al. (2020), for pure observational estimates see Koenig et al. (2014) and Donohue et al. (2016); and Florida–Bahamas Strait transport come from Larsen and Sanford (1985)

Name	obs	control	L_T	$0.5 \cdot L_T$	E_{eff}	L_T and E_{eff}	$0.5 \cdot L_T$ and E_{eff}
Barents Opening	2.1 Sv	2.4 Sv	0%	1%	4%	6%	7%
Bering Strait	1.0 Sv	0.7 Sv	2%	3%	5%	7%	8%
Canadian Arctic	-1.7 Sv	-1.6 Sv	4%	8%	14%	15%	16%
Fram Strait	-2.2 Sv	-1.3 Sv	-3%	-6%	-9%	-6%	-6%
Drake Passage (ACC)	157.3 Sv	152 Sv	0%	1%	4%	5%	7%
Florida–Bahamas Strait	32 Sv	13.2 Sv	1%	3%	4%	5%	6%

Acknowledgments

This work was funded in part by the two Research Council of Norway projects KeyClim (295046) and TopArctic (314826). A. Nummelin would like to thank Mats Bentsen for the help with the initial model setup.

References

Abernathey, R., & Cessi, P. (2014). Topographic enhancement of eddy efficiency in baroclinic equilibrium. *J. Phys. Oceanogr.*, *44*, 2017–2126.

Abernathey, R., Ferreira, D., & Klocker, A. (2013). Diagnostics of isopycnal mixing in a circumpolar channel. *Ocean Modelling*, *72*, 1 - 16. Retrieved from http://www.sciencedirect.com/science/article/pii/S1463500313001200 doi: https://doi.org/10.1016/j.ocemod.2013.07.004

Bachman, S. D. (2019). The GM+E closure: A framework for coupling backscatter with the Gent and McWilliams parameterization. *Ocean Modelling*, *136*, 85 - 106. Retrieved from http://www.sciencedirect.com/science/article/pii/S1463500318301975 doi: https://doi.org/10.1016/j.ocemod.2019.02.006

Bachman, S. D., Fox-Kemper, B., & Bryan, F. O. (2020). A diagnosis of anisotropic eddy diffusion from a high-resolution global ocean model. *Journal of Advances in Modeling Earth Systems*, *12*(2), e2019MS001904. Retrieved from https://agupubs.onlinelibrary.wiley.com/doi/abs/10.1029/2019MS001904 doi: 10.1029/2019MS001904

Beszczynska-Möller, A., von Appen, W.-J., & Fahrbach, E. (2015). *Physical oceanography and current meter data from moorings F1-F14 and F15/F16 in the Fram Strait, 1997-2012* [data set]. PANGAEA. Retrieved from https://doi.org/10.1594/PANGAEA.150016 doi: 10.1594/PANGAEA.150016

Blumsack, S. L., & Gierasch, P. J. (1972). Mars: The effects of topography on baroclinic instability. *J. Atmos. Sci.*, *29*, 1081-1089.

Bretherton, F. P., & Haidvogel, D. (1976). Two-dimesional turbulence over topography. *J. Fluid. Mech.*, *78*, 129–154.

Brink, K. H. (2012). Baroclinic instability of an idealized tidal mixing front. *J. Mar. Res.*, *70*(4), 661–688.

Brink, K. H. (2016). Cross-shelf exchange. *Annual Review of Marine Science*, *8*(1), 59-78. Retrieved from https://doi.org/10.1146/annurev-marine-010814-015717 (PMID: 26747520) doi: 10.1146/annurev-marine-010814-015717

Buongiorno Nardelli, B. (2020). A multi-year time series of observation-based 3d horizontal and vertical quasi-geostrophic global ocean currents. *Earth System Science Data*, *12*(3), 1711–1723. Retrieved from https://essd.copernicus.org/articles/12/1711/2020/ doi: 10.5194/essd-12-1711-2020

Chang, P., Zhang, S., Danabasoglu, G., Yeager, S. G., Fu, H., Wang, H., ... Wu, L. (2020). An unprecedented set of high-resolution earth system simulations for understanding multiscale interactions in climate variability and change. *Journal of Advances in Modeling Earth Systems*, *12*(12), e2020MS002298. Retrieved from https://agupubs.onlinelibrary.wiley.com/doi/abs/10.1029/2020MS002298 (e2020MS002298 2020MS002298) doi: https://doi.org/10.1029/2020MS002298

Curry, B., Lee, C. M., Petrie, B., Moritz, R. E., & Kwok, R. (2014). Multiyear volume, liquid freshwater, and sea ice transports through davis strait, 2004–10. *Journal of Physical Oceanography*, *44*(4), 1244 - 1266. Retrieved from https://journals.ametsoc.org/view/journals/phoc/44/4/jpo-d-13-0177.1.xml doi: 10.1175/JPO-D-13-0177.1

de Boer, A. M., Gavilan Pascual-Ahuir, E., Stevens, D. P., Chafik, L., Hutchinson, D. K., Zhang, Q., ... Willmott, A. J. (2018). Interconnectivity between volume transports through arctic straits. *Journal of Geophysical Research: Oceans*, *123*(12), 8714-8729. Retrieved from https://

agupubs.onlinelibrary.wiley.com/doi/abs/10.1029/2018JC014320 doi: https://doi.org/10.1029/2018JC014320

de La Lama, M., Lacasce, J. H., & Fuhr, H. K. (2016). The vertical structure of ocean eddies. *Dynamics and Statistics of the Climate System*, *1*(1), 1–16. doi: 10.1093/climsys/dzw001

Donohue, K. A., Tracey, K. L., Watts, D. R., Chidichimo, M. P., & Chereskin, T. K. (2016). Mean antarctic circumpolar current transport measured in drake passage. *Geophysical Research Letters*, *43*(22), 11,760-11,767. Retrieved from https://agupubs.onlinelibrary.wiley.com/doi/abs/10.1002/2016GL070319 doi: https://doi.org/10.1002/2016GL070319

Döös, K., Nycander, J., & Coward, A. C. (2008). Lagrangian decomposition of the deacon cell. *Journal of Geophysical Research: Oceans*, *113*(C7). Retrieved from https://agupubs.onlinelibrary.wiley.com/doi/abs/10.1029/2007JC004351 doi: https://doi.org/10.1029/2007JC004351

Eady, E. T. (1949). Long waves and cyclone waves. *Tellus*, *1*(3), 33-52. Retrieved from https://onlinelibrary.wiley.com/doi/abs/10.1111/j.2153-3490.1949.tb01265.x doi: 10.1111/j.2153-3490.1949.tb01265.x

Eden, C. (2007). Eddy length scales in the North Atlantic Ocean. *J. Geophys. Res.*, *112*(C06004). doi: 10.1029/2006JC003901

Eden, C., & Greatbatch, R. J. (2008). Towards a mesoscale eddy closure. *Ocean Modelling*, *20*(3), 223 - 239. Retrieved from http://www.sciencedirect.com/science/article/pii/S1463500307001163 doi: https://doi.org/10.1016/j.ocemod.2007.09.002

Ferrari, R., & Nikurashin, M. (2010). Suppression of eddy diffusivity across jets in the southern ocean. *Journal of Physical Oceanography*, *40*(7), 1501-1519. doi: 10.1175/2010JPO4278.1

Fox-Kemper, B., Adcroft, A., ning, C. W. B., Chassignet, E. P., Curchitser, E., Danabasoglu, G., ... Yeager, S. G. (2019, feb). Challenges and prospects in ocean circulation models. *Frontiers in Marine Science*, *6*. doi: 10.3389/fmars.2019.00065

Fox-Kemper, B., Ferrari, R., & Hallberg, R. (2008). Parameterization of mixed layer eddies. part i: Theory and diagnosis. *Journal of Physical Oceanography*, *38*(6), 1145 - 1165. Retrieved from https://journals.ametsoc.org/view/journals/phoc/38/6/2007jpo3792.1.xml doi: https://doi.org/10.1175/2007JPO3792.1

Frajka-Williams, E., Ansorge, I. J., Baehr, J., Bryden, H. L., Chidichimo, M. P., Cunningham, S. A., ... Wilson, C. (2019). Atlantic meridional overturning circulation: Observed transport and variability. *Frontiers in Marine Science*, *6*. Retrieved from https://www.frontiersin.org/articles/10.3389/fmars.2019.00260 doi: 10.3389/fmars.2019.00260

Fratantoni, D. M. (2001). North Atlantic surface circulation during the 1990's observed with satellite-tracked drifters. *Journal of Geophysical Research: Oceans (1978–2012)*, *106*(C10), 22067–22093.

Gent, P. R. (2011). The gent–mcwilliams parameterization: 20/20 hindsight. *Ocean Modelling*, *39*(1), 2 - 9. Retrieved from https://doi.org/10.1016/j.ocemod.2010.08.002 doi: 0.1016/j.ocemod.2010.08.002

Gent, P. R., & Mcwilliams, J. C. (1990). Isopycnal mixing in ocean circulation models. *Journal of Physical Oceanography*, *20*(1), 150-155. Retrieved from https://doi.org/10.1175/1520-0485(1990)020<0150:IMIOCM>2.0.CO;2 doi: 10.1175/1520-0485(1990)020⟨0150:IMIOCM⟩2.0.CO;2

Gent, P. R., Willebrand, J., McDougall, T. J., & McWilliams, J. C. (1995). Parameterizing eddy-induced tracer transports in ocean circulation models. *Journal of Physical Oceanography*, *25*(4), 463-474. Retrieved from https://doi.org/10.1175/1520-0485(1995)025<0463:PEITTI>2.0.CO;2 doi: 10.1175/1520-0485(1995)025⟨0463:PEITTI⟩2.0.CO;2

Green, J. S. (1970). Transfer properties of the large-scale eddies and the general circulation of the atmosphere. *Quart. J. Roy. Meteor. Soc.*, *96*, 157–185.

Haidvogel, D. B., & Brink, K. H. (1986). Mean currents driven by topographic drag over the continental shelf and slope. *J. Phys. Oceanogr.*, *16*, 2159–2171.

Hallberg, R. (2013). Using a resolution function to regulate parameterizations of oceanic mesoscale eddy effects. *Ocean Modelling*, *72*, 92 - 103. Retrieved from `https://doi.org/10.1016/j.ocemod.2013.08.007` doi: 10.1016/j.ocemod.2013.08.007

Hetland, R. D. (2017). Suppression of baroclinic instabilities in buoyancy-driven flow over sloping bathymetry. *J. Phys. Oceanogr.*, *47*(1). doi: 10.1175/JPO-D-15-0240.1

Holmes, R. M., Groeskamp, S., Stewart, K. D., & McDougall, T. J. (2022). Sensitivity of a coarse-resolution global ocean model to a spatially variable neutral diffusivity. *Journal of Advances in Modeling Earth Systems*, *14*(3), e2021MS002914. Retrieved from `https://agupubs.onlinelibrary.wiley.com/doi/abs/10.1029/2021MS002914` (e2021MS002914 2021MS002914) doi: https://doi.org/10.1029/2021MS002914

Ingvaldsen, R. B., Asplin, L., & Loeng, H. (2004). Velocity field of the western entrance to the barents sea. *Journal of Geophysical Research: Oceans*, *109*(C3). Retrieved from `https://agupubs.onlinelibrary.wiley.com/doi/abs/10.1029/2003JC001811` doi: https://doi.org/10.1029/2003JC001811

Isachsen, P. E. (2011). Baroclinic instability and eddy tracer transport across sloping bottom topography: How well does a modified eady model do in primitive equation simulations? *Ocean Modelling*, *39*(1), 183-199. Retrieved from `https://www.sciencedirect.com/science/article/pii/S1463500310001460` (Modelling and Understanding the Ocean Mesoscale and Submesoscale) doi: https://doi.org/10.1016/j.ocemod.2010.09.007

Jansen, M. F., Adcroft, A., Khani, S., & Kong, H. (2019). Toward an Energetically Consistent, Resolution Aware Parameterization of Ocean Mesoscale Eddies. *Journal of Advances in Modeling Earth Systems*, *0*(0). Retrieved from `https://agupubs.onlinelibrary.wiley.com/doi/abs/10.1029/2019MS001750` doi: 10.1029/2019MS001750

Jansen, M. F., Adcroft, A. J., Hallberg, R., & Held, I. M. (2015). Parameterization of eddy fluxes based on a mesoscale energy budget. *Ocean Mod.*, *92*, 28–41.

Khani, S., Jansen, M. F., & Adcroft, A. (2019). Diagnosing subgrid mesoscale eddy fluxes with and without topography. *J. Adv. Mod. Earth Sci.*, *11*, 3995–4015. doi: 10.1029/2019MS001721

Killworth, P. D. (1992). An equivalent-barotropic mode in the Fine Resolution Antarctic Model. *J. Phys. Oceanogr.*, *22*, 1379–1387. doi: 10.1175/1520-0485(1992)022

Kjellsson, J., & Zanna, L. (2017). The impact of horizontal resolution on energy transfers in global ocean models. *Fluids*, *2*(3). Retrieved from `https://www.mdpi.com/2311-5521/2/3/45` doi: 10.3390/fluids2030045

Klocker, A., Ferrari, R., & LaCasce, J. H. (2012). Estimating suppression of eddy mixing by mean flows. *Journal of Physical Oceanography*, *42*(9), 1566–1576.

Koenig, Z., Provost, C., Ferrari, R., Sennéchael, N., & Rio, M.-H. (2014). Volume transport of the antarctic circumpolar current: Production and validation of a 20 year long time series obtained from in situ and satellite observations. *Journal of Geophysical Research: Oceans*, *119*(8), 5407-5433. Retrieved from `https://agupubs.onlinelibrary.wiley.com/doi/abs/10.1002/2014JC009966` doi: https://doi.org/10.1002/2014JC009966

Koszalka, I., LaCasce, J., Andersson, M., Orvik, K., & Mauritzen, C. (2011). Surface circulation in the Nordic Seas from clustered drifters. *Deep-Sea Res. I*, *58*, 468–485.

LaCasce, J. H. (2000). Floats and f/H. *J. Mar. Res.*, *58*, 61–95.

Lacasce, J. H. (2017). The Prevalence of oceanic surface modes. *Geophys. Res. Lettr.*, *44*(21), 11097–11105. doi: 10.1002/2017GL075430

Lacasce, J. H., & Brink, K. (2000). Geostrophic turbulence over a slope. *J. Phys. Oceanogr.*, *30*, 1305–1324.

Larsen, J. C., & Sanford, T. B. (1985). Florida current volume transports from voltage measurements. *Science*, *227*(4684), 302-304. Retrieved from https://www.science.org/doi/abs/10.1126/science.227.4684.302 doi: 10.1126/science.227.4684.302

Locarnini, R. A., Mishonov, A. V., Baranova, O. K., Boyer, T. P., Zweng, M. M., Garcia, H. E., ... Smolyar, I. (2018). *World ocean atlas 2018, volume 1: Temperature. a. mishonov technical ed.* NOAA Atlas NESDIS 81, 52pp. Retrieved from https://www.ncei.noaa.gov/sites/default/files/2022-06/woa18_vol1.pdf

Lumpkin, R., & Speer, K. (2007). Global ocean meridional overturning. *Journal of Physical Oceanography*, *37*(10), 2550 - 2562. Retrieved from https://journals.ametsoc.org/view/journals/phoc/37/10/jpo3130.1.xml doi: https://doi.org/10.1175/JPO3130.1

Mak, J., Maddison, J. R., Marshall, D. P., & Munday, D. R. (2018). Implementation of a geometrically informed and energetically constrained mesoscale eddy parameterization in an ocean circulation model. *Journal of Physical Oceanography*, *0*(0), null. Retrieved from https://doi.org/10.1175/JPO-D-18-0017.1 doi: 10.1175/JPO-D-18-0017.1

Manucharyan, G. E., & Isachsen, P. E. (2019). Critical Role of Continental Slopes in Halocline and Eddy Dynamics of the Ekman-Driven Beaufort Gyre. *J. Geophys. Res.*, *124*, 2679–2696. doi: 10.1029/2018JC014624

Manucharyan, G. E., & Stewart, A. L. (2022). Stirring of interior potential porticity gradients as a formation mechanism for large subsurface-intensified eddies in the Beaufort Gyre. *J. Phys. Oceanogr.*, *52*, 3349–3370.

Marshall, D. P., Maddison, J. R., & Berloff, P. S. (2012). A framework for parameterizing eddy potential vorticity fluxes. *Journal of Physical Oceanography*, *42*(4), 539-557. Retrieved from https://doi.org/10.1175/JPO-D-11-048.1 doi: 10.1175/JPO-D-11-048.1

Mechoso, C. R. (1980). Baroclinic instability of flows along sloping boundaries. *J. Atmos. Sci.*, *37*, 1393–1399.

Meneghello, G., Marshall, J., Lique, C., Isachsen, P. E., Doddridge, E., Campin, J.-M., ... Talandier, C. (2021). Genesis and decay of mesoscale baroclinic eddies in the seasonally ice-covered interior arctic ocean. *Journal of Physical Oceanography*, *51*(1), 115 - 129. Retrieved from https://journals.ametsoc.org/view/journals/phoc/51/1/jpo-d-20-0054.1.xml doi: 10.1175/JPO-D-20-0054.1

Nummelin, A., Busecke, J. J. M., Haine, T. W. N., & Abernathey, R. P. (2021). Diagnosing the scale- and space-dependent horizontal eddy diffusivity at the global surface ocean. *Journal of Physical Oceanography*, *51*(2), 279 - 297. Retrieved from https://journals.ametsoc.org/view/journals/phoc/51/2/jpo-d-19-0256.1.xml doi: 10.1175/JPO-D-19-0256.1

Nøst, O. A., & Isachsen, P. E. (2003). The large-scale time-mean ocean circulation in the Nordic Seas and Arctic Ocean estimated from simplified dynamics. *J. Mar. Res.*, *61*, 175-210.

Prandtl, L. (1925, January). 7. Bericht über Untersuchungen zur ausgebildeten Turbulenz. *Zeitschrift Angewandte Mathematik und Mechanik*, *5*(2), 136-139. doi: 10.1002/zamm.19250050212

Redi, M. H. (1982). Oceanic isopycnal mixing by coordinate rotation. *Journal of Physical Oceanography*, *12*(10), 1154-1158. Retrieved from https://doi.org/10.1175/1520-0485(1982)012<1154:OIMBCR>2.0.CO;2 doi: 10.1175/1520-0485(1982)012⟨1154:OIMBCR⟩2.0.CO;2

Rhines, P. (1977). The dynamics of unsteady currents. In *The sea* (Vol. 6, p. 189–318). New York: Wiley.

Seland, Ø., Bentsen, M., Olivié, D., Toniazzo, T., Gjermundsen, A., Graff, L. S., ... Schulz, M. (2020). Overview of the norwegian earth system model (noresm2) and key climate response of cmip6 deck, historical, and scenario simulations. *Geoscientific Model Development*, *13*(12), 6165–6200. Retrieved from https://gmd.copernicus.org/articles/13/6165/2020/ doi: 10.5194/gmd-13-6165-2020

Smith, K. S., & Marshall, J. (2009). Evidence for Enhanced Eddy Mixing at Middepth in the Southern Ocean. *Journal of Physical Oceanography*, *39*(1), 50-69. Retrieved from https://doi.org/10.1175/2008JPO3880.1 doi: 10.1175/2008JPO3880.1

Smith, R. D., & Gent, P. R. (2004). Anisotropic gent–mcwilliams parameterization for ocean models. *Journal of Physical Oceanography*, *34*(11), 2541-2564. Retrieved from https://doi.org/10.1175/JPO2613.1 doi: 10.1175/JPO2613.1

Speer, K., Rintoul, S. R., & Sloyan, B. (2000). The diabatic deacon cell. *Journal of Physical Oceanography*, *30*(12), 3212 - 3222. Retrieved from https://journals.ametsoc.org/view/journals/phoc/30/12/1520-0485_2000_030_3212_tddc_2.0.co_2.xml doi: https://doi.org/10.1175/1520-0485(2000)030⟨3212:TDDC⟩2.0.CO;2

Stammer, D. (1997). Global Characteristics of Ocean Variability Estimated from Regional TOPEX/POSEIDON Altimeter Measurements. *J. Phys. Oceanogr.*, *27*, 1743–1769.

Stanley, Z., Bachman, S. D., & Grooms, I. (2020). Vertical structure of ocean mesoscale eddies with implications for parameterizations of tracer transport. *Journal of Advances in Modeling Earth Systems*, *12*(10), e2020MS002151. Retrieved from https://agupubs.onlinelibrary.wiley.com/doi/abs/10.1029/2020MS002151 doi: https://doi.org/10.1029/2020MS002151

Stewart, A. L., Neumann, N. K., & Solodoch, A. (2023). "Eddy" saturation of the Antarctic Circumpolar Current by standing waves. *J. Phys. Oceanogr.*. doi: 10.1175/JPO-D-22-0154.1

Stewart, K., Spence, P., Waterman, S., Sommer, J. L., Molines, J.-M., Lilly, J., & England, M. (2015). Anisotropy of eddy variability in the global ocean. *Ocean Modelling*, *95*, 53-65. Retrieved from https://www.sciencedirect.com/science/article/pii/S1463500315001638 doi: https://doi.org/10.1016/j.ocemod.2015.09.005

Stone, P. (1972). A simplified radiative-dynamical model for the static stability of rotating atmospheres. *J. Atmos. Sci.*, *29*, 405-418.

Sutyrin, G. G., Radko, T., & Nycander, J. (2021). Steady radiating baroclinic vortices in vertically sheared flows. *Physics of Fluids*, *33*(3), 031705. Retrieved from https://doi.org/10.1063/5.0040298 doi: 10.1063/5.0040298

Trenberth, K. E., Zhang, Y., Fasullo, J. T., & Cheng, L. (2019). Observation-based estimates of global and basin ocean meridional heat transport time series. *Journal of Climate*, *32*(14), 4567 - 4583. Retrieved from https://journals.ametsoc.org/view/journals/clim/32/14/jcli-d-18-0872.1.xml doi: https://doi.org/10.1175/JCLI-D-18-0872.1

Trodahl, M., & Isachsen, P. E. (2018). Topographic influence on baroclinic instability and the mesoscale eddy field in the northern north atlantic ocean and the nordic seas. *Journal of Physical Oceanography*, *48*(11), 2593 - 2607. Retrieved from https://journals.ametsoc.org/view/journals/phoc/48/11/jpo-d-17-0220.1.xml doi: 10.1175/JPO-D-17-0220.1

Tsujino, H., Urakawa, L. S., Griffies, S. M., Danabasoglu, G., Adcroft, A. J., Amaral, A. E., ... Yu, Z. (2020). Evaluation of global ocean–sea-ice model simulations based on the experimental protocols of the ocean model intercomparison

project phase 2 (omip-2). *Geoscientific Model Development*, *13*(8), 3643–3708. Retrieved from https://gmd.copernicus.org/articles/13/3643/2020/ doi: 10.5194/gmd-13-3643-2020

Uchida, T., Jamet, Q., Dewar, W. K., Le Sommer, J., Penduff, T., & Balwada, D. (2022). Diagnosing the thickness-weighted averaged eddy-mean flow interaction from an eddying north atlantic ensemble: The eliassen-palm flux. *Journal of Advances in Modeling Earth Systems*, *14*(5), e2021MS002866. Retrieved from https://agupubs.onlinelibrary.wiley.com/doi/abs/10.1029/2021MS002866 (e2021MS002866 2021MS002866) doi: https://doi.org/10.1029/2021MS002866

Vallis, G., & Maltrud, M. E. (1993). Generation of mean flows and jets on a beta-plane and over topography. *J. Phys. Oceanogr.*, *23*, 1346-1362.

Visbeck, M., Marshall, J., Haine, T., & Spall, M. (1997). Specification of eddy transfer coefficients in coarse-resolution ocean circulation models. *Journal of Physical Oceanography*, *27*(3), 381-402. Retrieved from https://doi.org/10.1175/1520-0485(1997)027<0381:SOETCI>2.0.CO;2 doi: 10.1175/1520-0485(1997)027⟨0381:SOETCI⟩2.0.CO;2

Wang, Y., & Stewart, A. L. (2018). Eddy dynamics over continental slopes under retrograde winds: Insights from a model inter-comparison. *Ocean Modelling*, *121*, 1-18. Retrieved from https://www.sciencedirect.com/science/article/pii/S146350031730183X doi: https://doi.org/10.1016/j.ocemod.2017.11.006

Wang, Y., & Stewart, A. L. (2020). Scalings for eddy buoyancy transfer across continental slopes under retrograde winds. *Ocean Modelling*, *147*, 101579. Retrieved from https://www.sciencedirect.com/science/article/pii/S1463500319301775 doi: https://doi.org/10.1016/j.ocemod.2020.101579

Wei, H., & Wang, Y. (2021). Full-depth scalings for isopycnal eddy mixing across continental slopes under upwelling-favorable winds. *Journal of Advances in Modeling Earth Systems*, *13*(6), e2021MS002498. Retrieved from https://agupubs.onlinelibrary.wiley.com/doi/abs/10.1029/2021MS002498 doi: https://doi.org/10.1029/2021MS002498

Wei, H., Wang, Y., Stewart, A. L., & Mak, J. (2022). Scalings for eddy buoyancy fluxes across prograde shelf/slope fronts. *Journal of Advances in Modeling Earth Systems*, *14*(12), e2022MS003229. Retrieved from https://agupubs.onlinelibrary.wiley.com/doi/abs/10.1029/2022MS003229 (e2022MS003229 2022MS003229) doi: https://doi.org/10.1029/2022MS003229

Woodgate, R. A. (2018). Increases in the pacific inflow to the arctic from 1990 to 2015, and insights into seasonal trends and driving mechanisms from year-round bering strait mooring data. *Progress in Oceanography*, *160*, 124-154. Retrieved from https://www.sciencedirect.com/science/article/pii/S0079661117302215 doi: https://doi.org/10.1016/j.pocean.2017.12.007

Woodgate, R. A., Stafford, K. M., & Prahl, F. G. (2015). A synthesis of year-round interdisciplinary mooring measurements in the bering strait (1990–2014) and the rusalca years (2004–2011). *Oceanography*. Retrieved from https://doi.org/10.5670/oceanog.2015.57

Wunsch, C. (1997). The vertical partition of oceanic horizontal kinetic energy. *J. Phys. Oceanogr.*, *27*, 1770–1794.

Xu, X., Chassignet, E. P., Firing, Y. L., & Donohue, K. (2020). Antarctic circumpolar current transport through drake passage: What can we learn from comparing high-resolution model results to observations? *Journal of Geophysical Research: Oceans*, *125*(7), e2020JC016365. Retrieved from https://agupubs.onlinelibrary.wiley.com/doi/abs/10.1029/2020JC016365 (e2020JC016365 2020JC016365) doi: https://doi.org/10.1029/2020JC016365

Yankovsky, E., Zanna, L., & Smith, K. S. (2022). Influences of mesoscale ocean ed-

dies on flow vertical structure in a resolution-based model hierarchy. *Journal of Advances in Modeling Earth Systems*, *14*(11), e2022MS003203. Retrieved from https://agupubs.onlinelibrary.wiley.com/doi/abs/10.1029/2022MS003203 (e2022MS003203 2022MS003203) doi: https://doi.org/10.1029/2022MS003203

Zhang, W., & Wolfe, C. L. P. (2022). On the vertical structure of oceanic mesoscale tracer diffusivities. *Journal of Advances in Modeling Earth Systems*, *14*(6), e2021MS002891. Retrieved from https://agupubs.onlinelibrary.wiley.com/doi/abs/10.1029/2021MS002891 (e2021MS002891 2021MS002891) doi: https://doi.org/10.1029/2021MS002891

Zweng, M. M., Reagan, J. R., Seidov, D., Boyer, T. P., Locarnini, R. A., Garcia, H. E., ... Smolyar, I. (2018). *World ocean atlas 2018, volume 2: Salinity. a. mishonov technical ed.* NOAA Atlas NESDIS 82, 50pp. Retrieved from https://www.ncei.noaa.gov/sites/default/files/2022-06/woa18_vol2.pdf

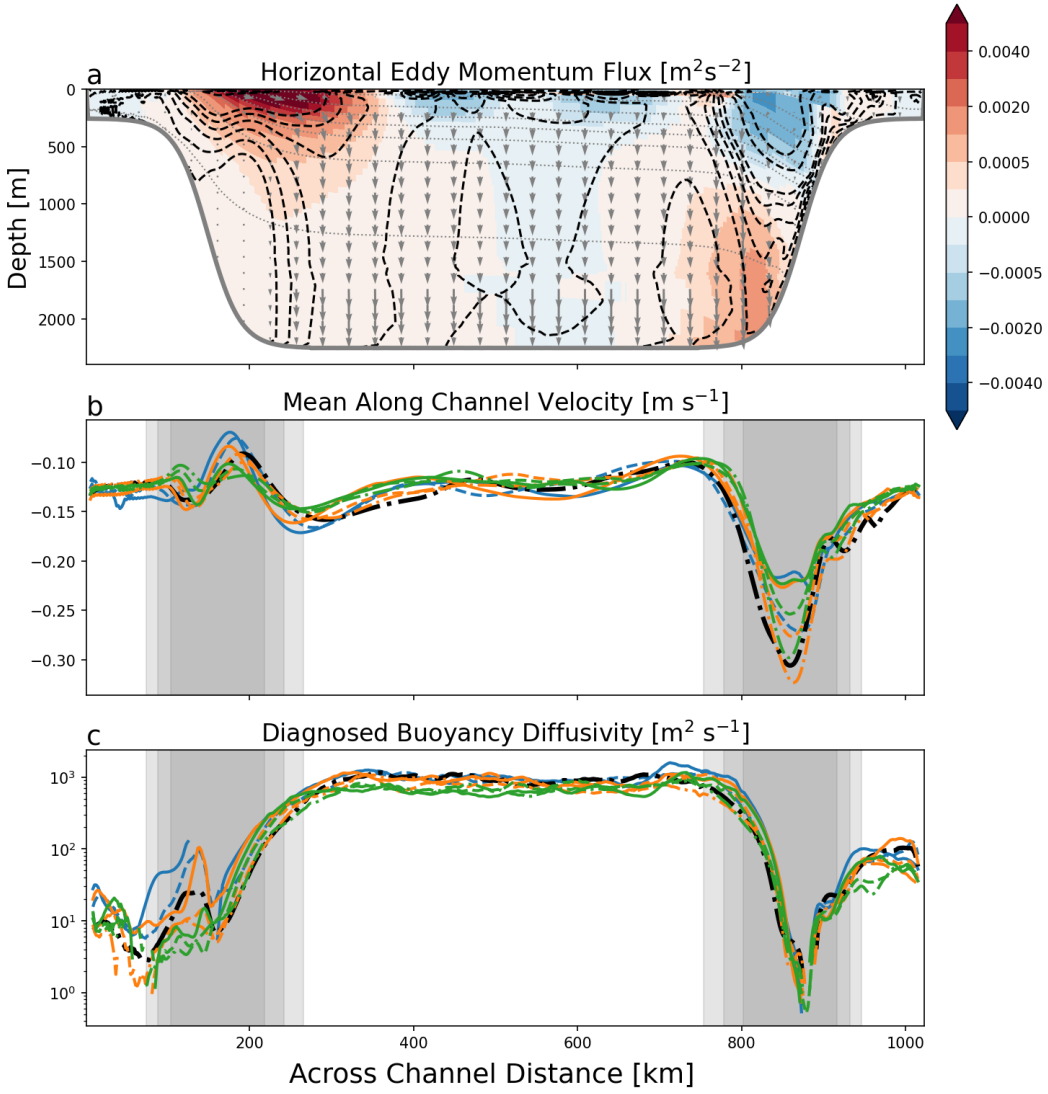

Figure 1. Cross section of zonally and temporally-averaged (a) horizontal eddy momentum flux (shading), E-P flux (gray arrows), mean velocity (dashed black contours), and mean density (dotted gray contours), (b) vertically-averaged along-channel velocity and (c) vertically-averaged meridional buoyancy (temperature) diffusivity. In panels b and c we indicate stratification by color (in descending order: blue, orange, green) and slope width (steepness) by line-style (in descending order: dashed-dotted, dashed, solid). The black line is experiment 3 (Table 2) and corresponds to the case shown in panel a. Gray shading shows the location of the slope regions in the different simulations (where $300m < H < 2250m$). For some of the simulations the diffusivity lines are broken because of negative diffusivities that are not shown on the log scale.

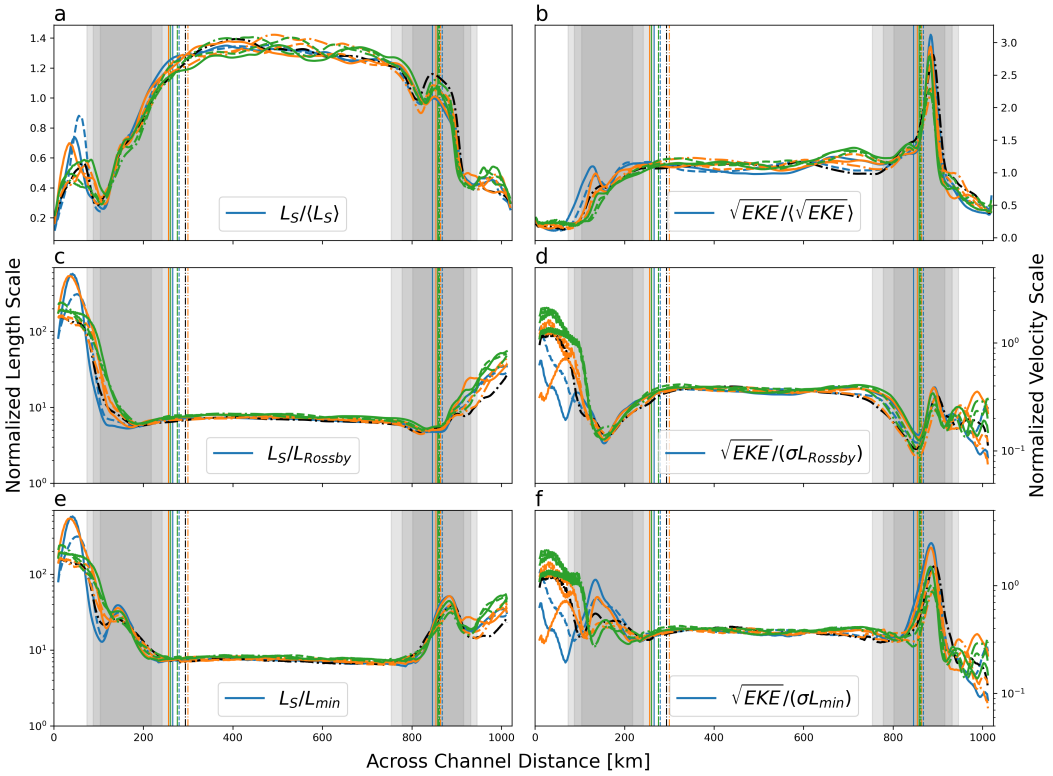

Figure 2. Diagnosed length scales (panels on the left) and velocity scales (panels on the right) for all experiments. All measures have been normalized. The top row (panels a and b) are normalized by the basin mean values. Length scales in panel c and panel e are normalized by the deformation radius and by the mimimum of the deformation radius and topographic Rhines scale, respectively. In panels d and f we normalize by the parameterized velocity scale, using length scales from c and e, respectively. Colors and line styles as in Fig. 1. Gray shadings indicate the slope regions (similar to Fig. 1) and vertical lines indicate the location of maxima in depth-averaged velocity in each experiment.

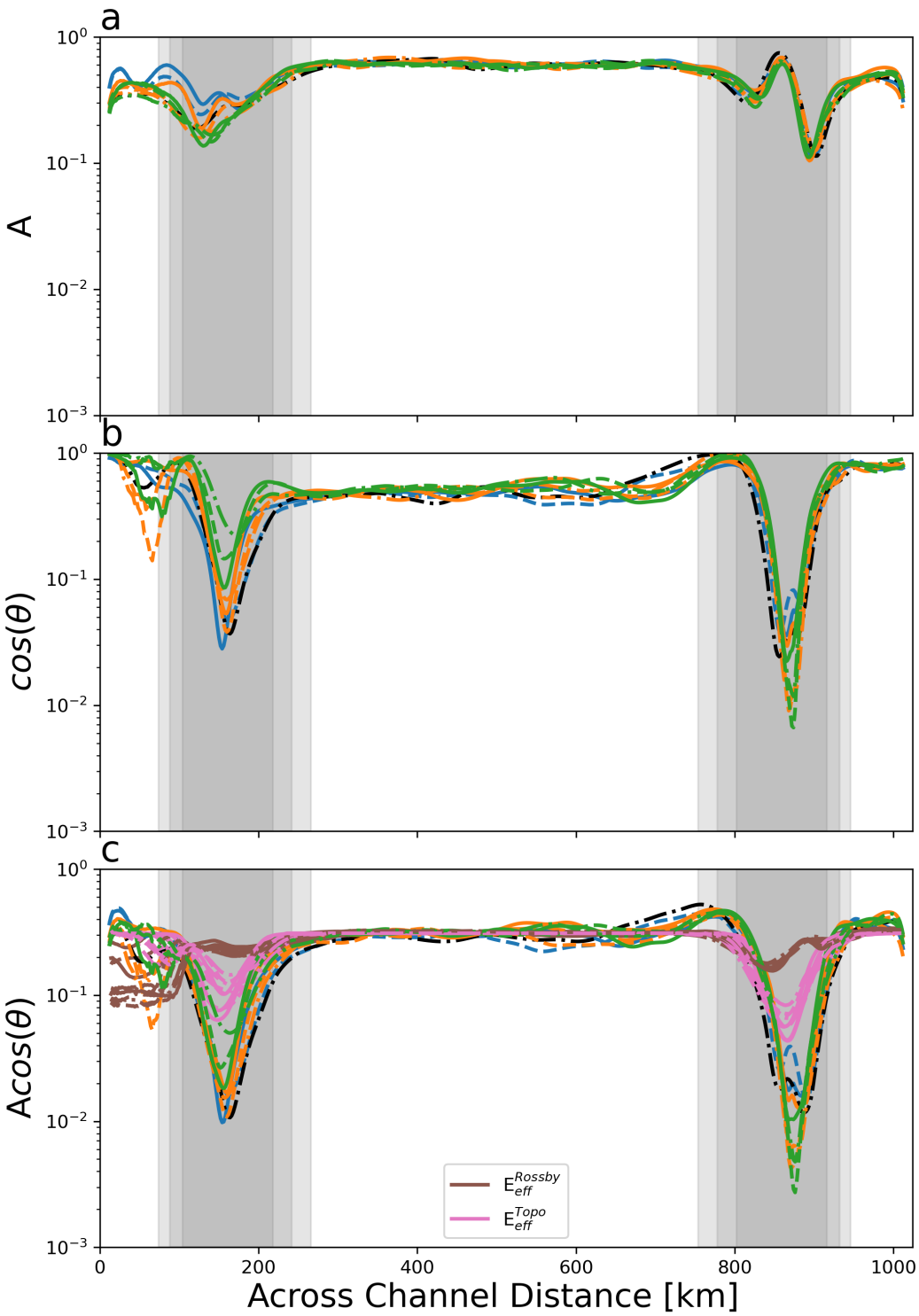

Figure 3. Measures of anisotropy and phase angle relationships: (a) eddy velocity anisotropy (A), (b) cosine of the phase angle between T' and v' and (c) the product of (a) and (b), as well as the parameterized eddy efficiency factors E_{eff} (brown when using deformation radius, pink when using the topographic Rhines scale). For the two E_{eff} estimates we use $a_2 = 10$ and$a_1 = 0.35$ and $a_1 = 0.32$, respectively, to match the mid-basin values of $A\cos(\theta)$. Colors and line styles for the diagnosed cases as in Fig. 1, and gray shadings indicate the slope regions (similar to Fig. 1)

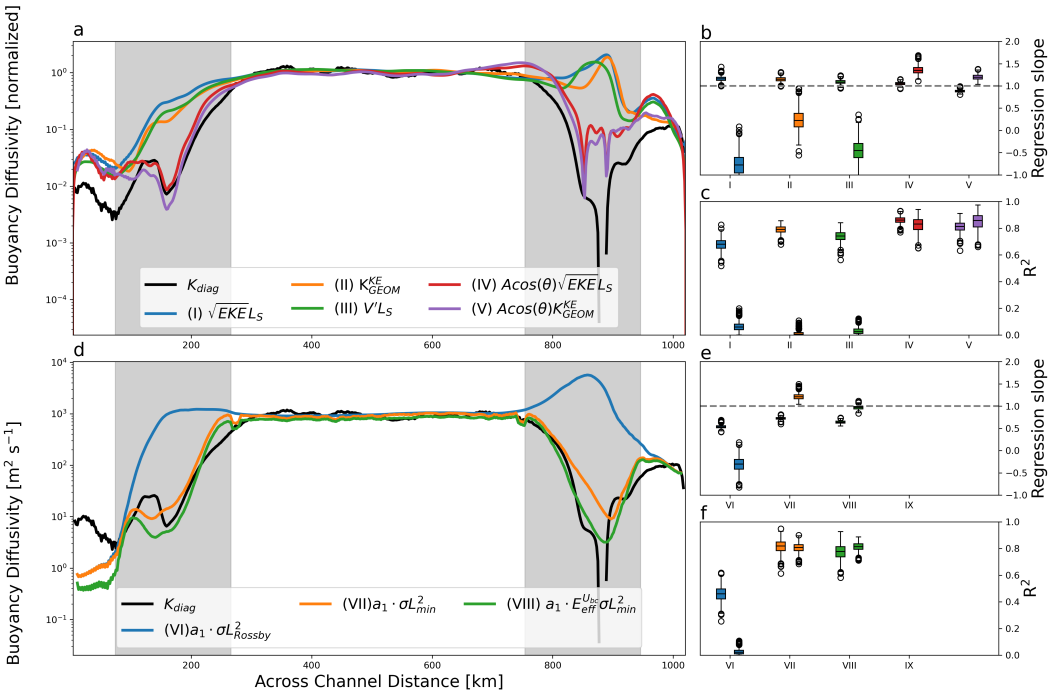

Figure 4. Partly-parameterized (a–c) and fully-parameterized (d–e) across-slope buoyancy diffusivities. The left panels show across-basin profiles for experiment 3 (Table 2) whereas the right panels summarize the statistics of linear fits between the diagnosed and parameterized diffusivities across all experiments (b–c, e–f; statistics are from a linear regression using 200 points across all cases that is repeated 5000 times). Boxes and whiskers come in pairs, with the left and right ones corresponding to the southern and northern slope, respectively. Linear regressions are done over the slope regions only (gray shading; similar to Fig. 1). Panel a shows diffusivities normalized by their basin mean value, whereas panel d shows absolute values. In panel d, $a_1 = 0.25$ for estimate VI, for VII–VIII $a_1 = 0.02$, and in VIII $a_2 = 10$.

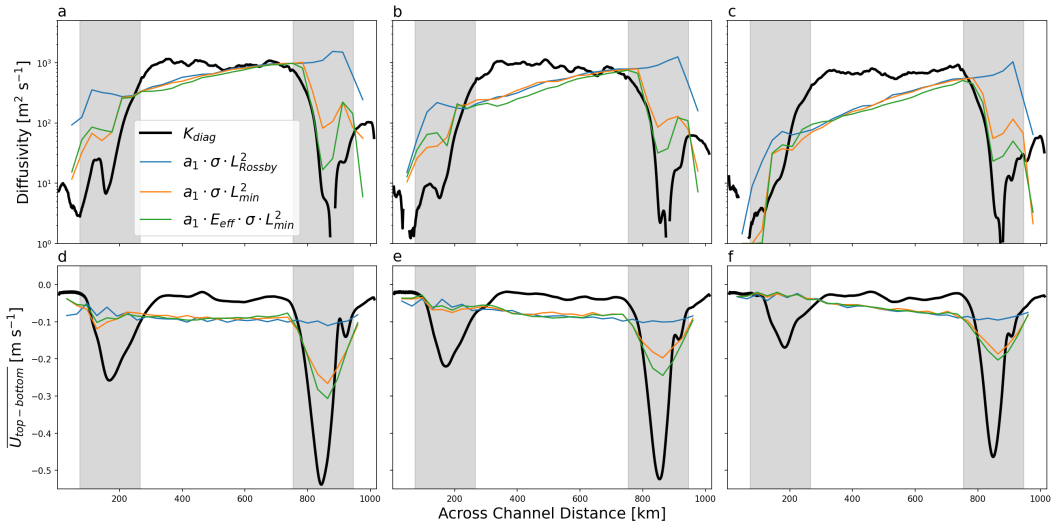

Figure 5. Buoyancy diffusivity (top panels) and top-to-bottom thermal wind shear (lower panels) in the coarse-resolution channel simulation compared to the high-resolution simulation (thick black line). The different columns are separated by stratification such that the initial conditions are the same as for Exp 3, 6 and 9 in the left, middle and right columns, respectively.

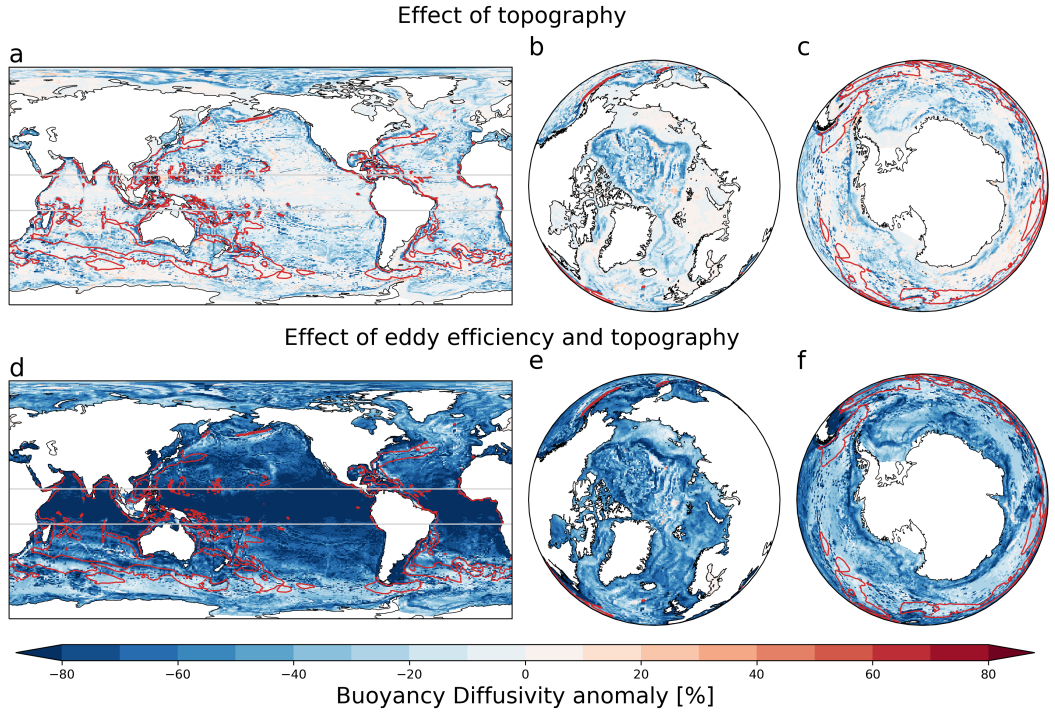

Figure 6. Anomalies from the control case in parameterized (depth-averaged) GM diffusivity due to implementation of (top row) the topographic Rhines scale and (bottom row) eddy efficiency in addition to the topograhic Rhines scale. Red contours show the 1000 m^2 s^{-1} isoline for diffusivity in the control case and light gray contours show areas in the tropics where the grid size is smaller than the internal deformation radius and therefore the resolution function (Hallberg, 2013) reducing the GM coefficient is in effect.

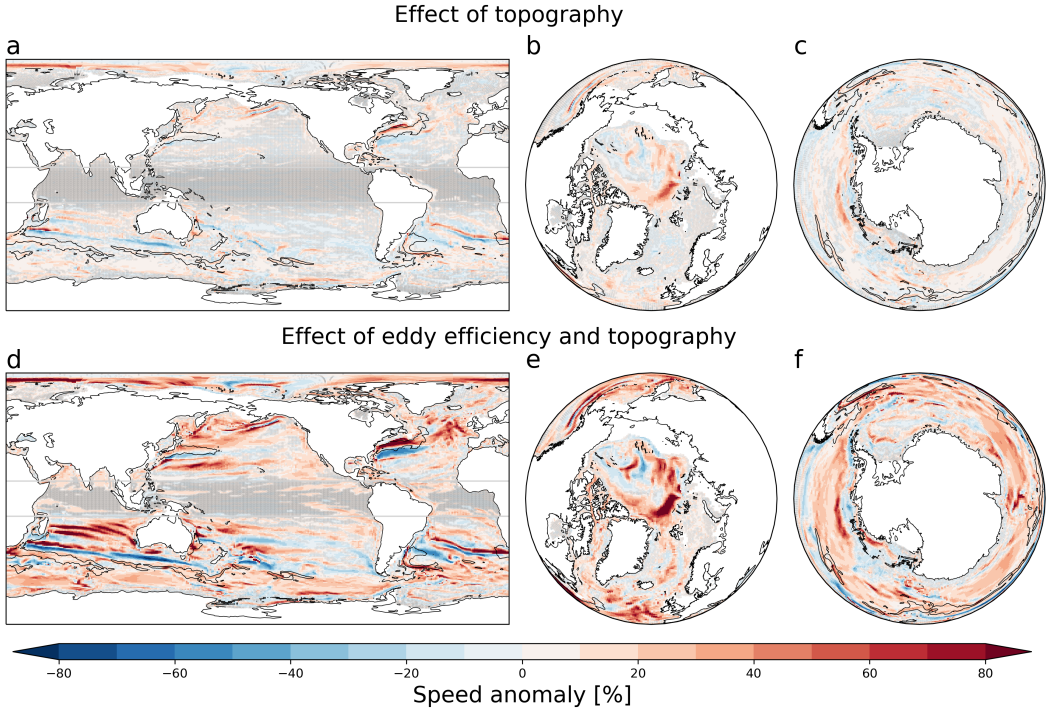

Figure 7. Flow speed anomalies from the control case at 100–200 m depth due to implementation of: (top row) the topographic Rhines scale and (bottom row) eddy efficiency in addition to the topograhic Rhines scale. Black contours show the 0.25 m s^{-1} isolines for observational estimate of the quasi-geostrophic current speed (Buongiorno Nardelli, 2020) in the same 100–200 m depth interval. Gray dots mark grid cells where the mean difference from the control case is not significant at the 5% level (student's t-test).

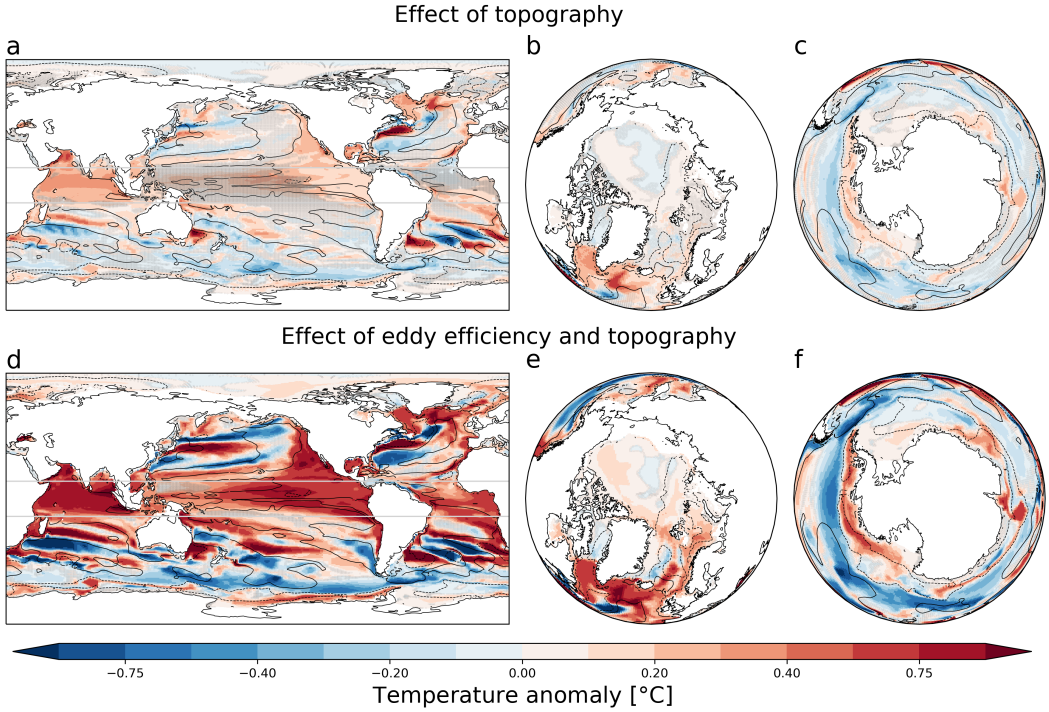

Figure 8. Temperature anomalies from the control case in resolved temperature field between 100–200 m depth due to implementation of: (top row) the topographic Rhines scale and (bottom row) eddy efficiency in addition to the topograhic Rhines scale. Black contours show the ±1°C (solid/dashed) isoline for the control case bias relative to the WOA observations. Therefore, whenever solid (dashed) contours surrounds blue (red) areas the bias is reduced. Gray dots mark grid cells where the mean difference from the control case is not significant at the 5% level (student's t-test).

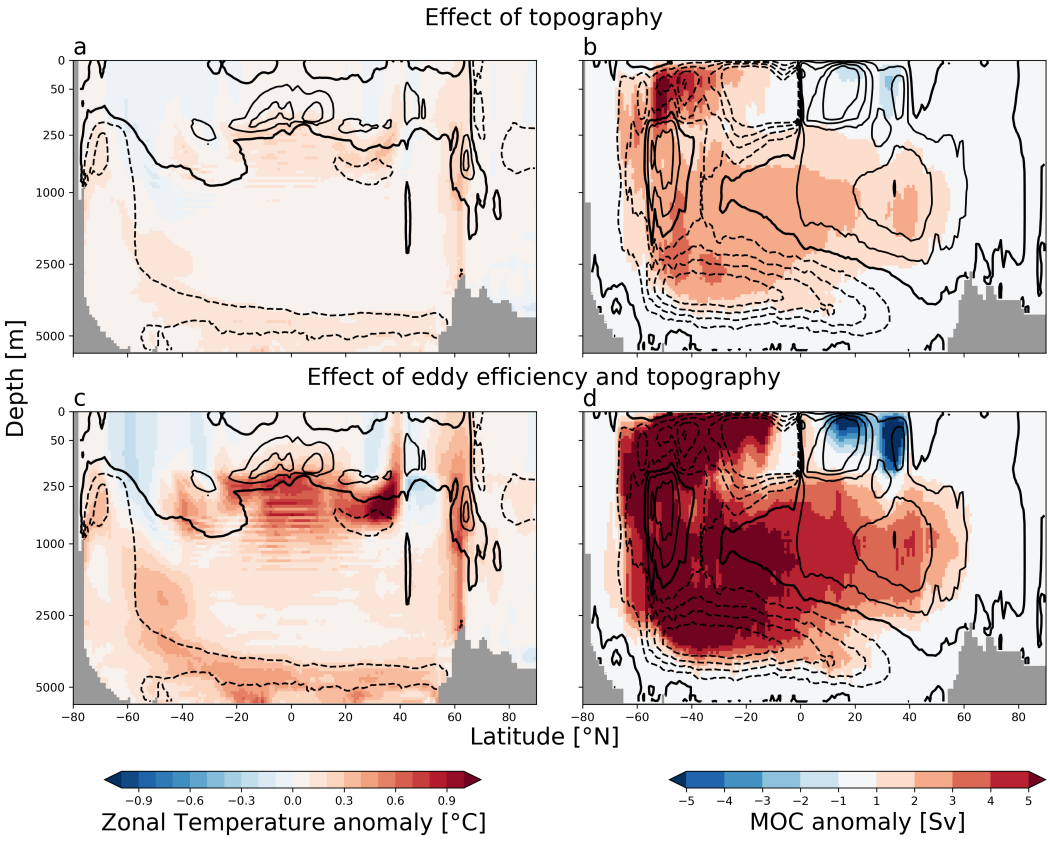

Figure 9. Zonal-mean temperature anomalies (left panels) and global meridional overturning stream function anomalies (right panels), relative to the control simulation, due to implementation of: (top row) the topographic Rhines scale and (bottom row) eddy efficiency in addition to the topograhic Rhines scale. For temperature, black contours show the control case bias relative to the WOA observations in 0.25°C intervals (dashed for negative, solid for positive, the thick solid curve shows the zero contour). Therefore, whenever solid (dashed) contours surround blue (red) areas the bias to the observations is reduced. For MOC the contours show the control case MOC at 5 Sv intervals with the thick solid curve indicating the 0 Sv contour. Therefore solid (dashed) contours surrounding red (blue) indicates intensifying overturning.

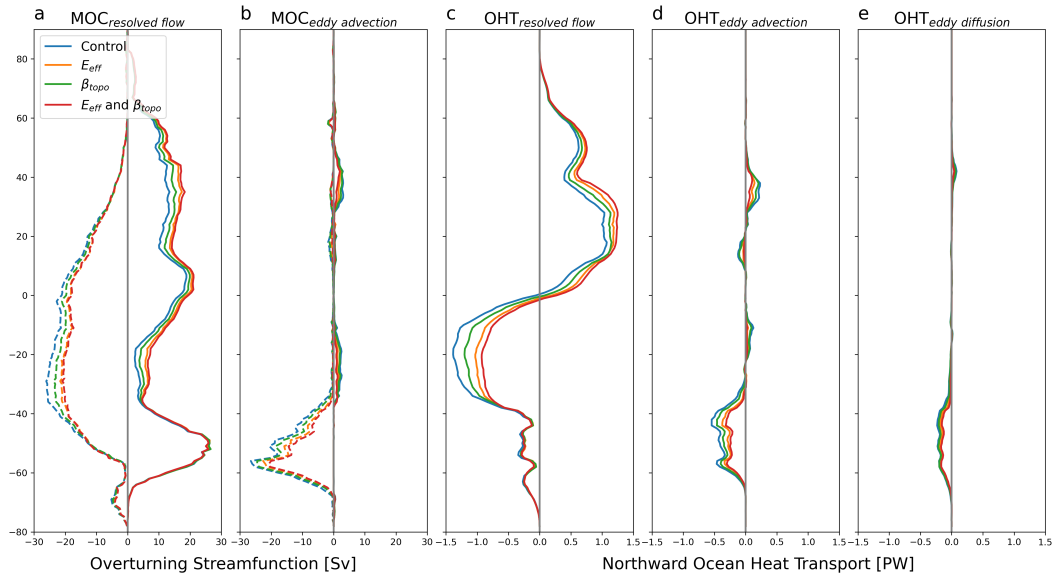

Figure 10. Resolved and eddy contributions to the global meridional overturning circulation (MOC, panels a and b) and to the global northward ocean heat transport (OHT, panels c–e). For the MOC we show the maximum (solid) and minimum (dashed) below 500 m to avoid the shallow surface overturning cells. For the OHT we show both advective and diffusive eddy contributions (panels d and e, respectively).

Figure 1.

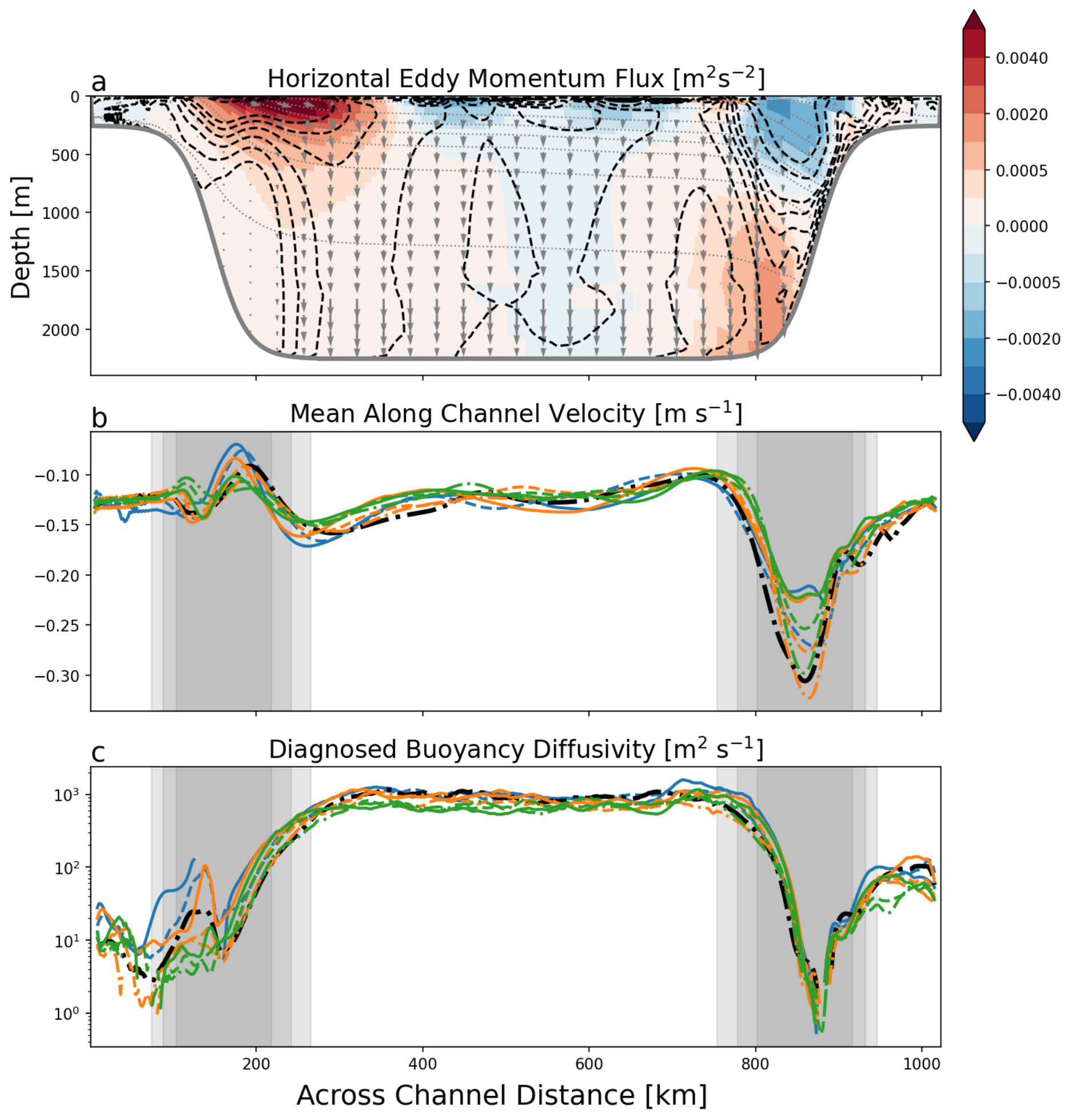
a
Horizontal Eddy Momentum Flux [m^{2}s^{-2}]
Depth [m]
0
500
1000
1500
2000
0.0040
0.0020
0.0005
0.0000
−0.0005
−0.0020
−0.0040
b
Mean Along Channel Velocity [m s^{-1}]
−0.10
−0.15
−0.20
−0.25
−0.30
c
Diagnosed Buoyancy Diffusivity [m^2 s^{-1}]
10^3
10^2
10^1
10^0
200
400
600
800
1000
Across Channel Distance [km]

Figure 2.

a

b

c

d

e

f

$L_S/\langle L_S \rangle$

$\sqrt{EKE}/\langle\sqrt{EKE}\rangle$

L_S/L_{Rossby}

$\sqrt{EKE}/(\sigma L_{Rossby})$

L_S/L_{min}

$\sqrt{EKE}/(\sigma L_{min})$

Normalized Length Scale

Normalized Velocity Scale

Across Channel Distance [km]

Figure 3.

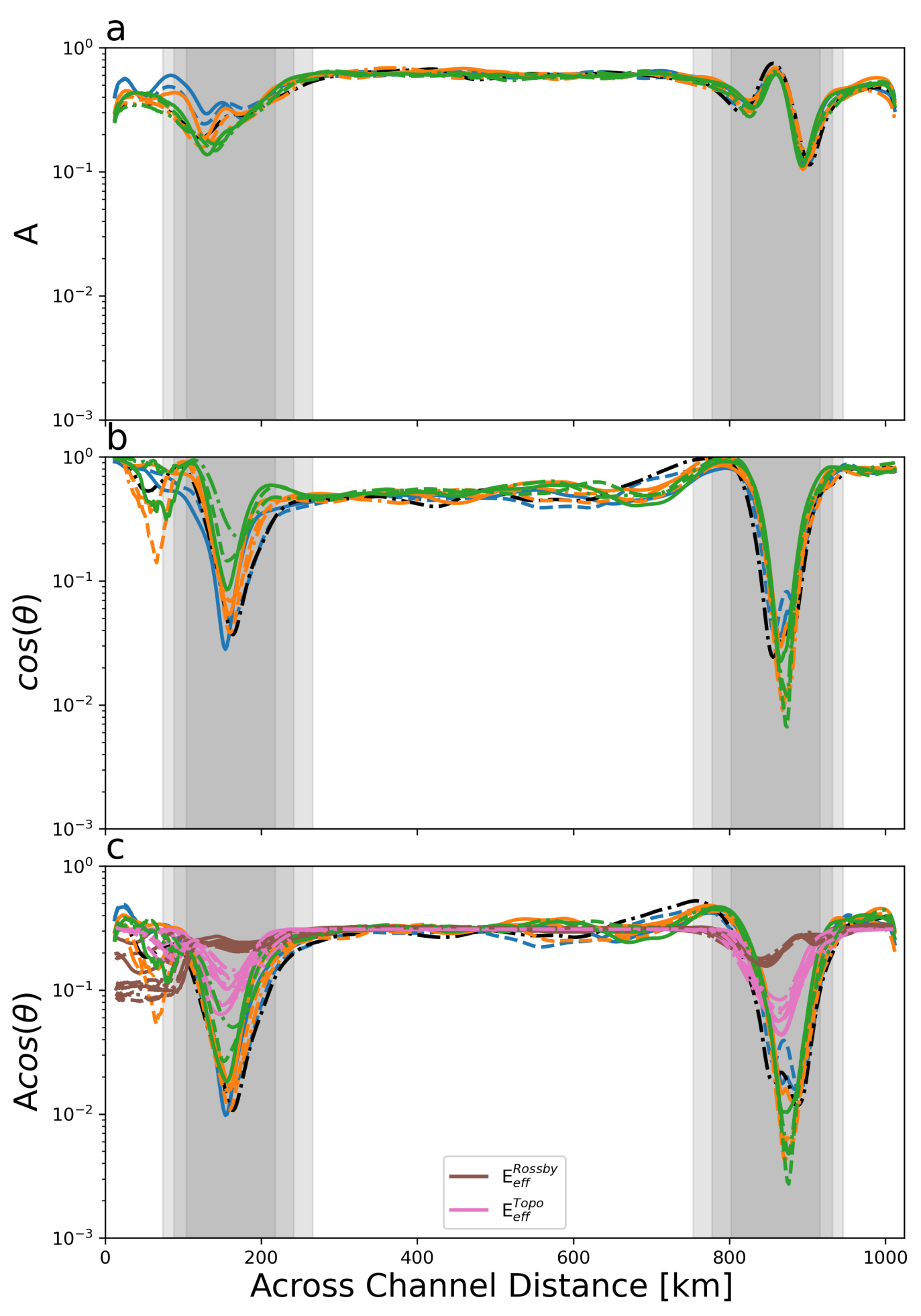
a
b
c
A
cos(θ)
Acos(θ)
10^0
10^-1
10^-2
10^-3
0
200
400
600
800
1000
Across Channel Distance [km]
E_eff^Rossby
E_eff^Topo

Figure 4.

a

b

c

d

e

f

Buoyancy Diffusivity [normalized]

Buoyancy Diffusivity [$m^2\ s^{-1}$]

Across Channel Distance [km]

Regression slope

R^2

K_{diag}

(I) $\sqrt{EKE}L_S$

(II) K^{KE}_{GEOM}

(III) $V'L_S$

(IV) $Acos(\theta)\sqrt{EKE}L_S$

(V) $Acos(\theta)K^{KE}_{GEOM}$

(VI) $a_1 \cdot \sigma L^2_{Rossby}$

(VII) $a_1 \cdot \sigma L^2_{min}$

(VIII) $a_1 \cdot E^{U_{bc}}_{eff} \sigma L^2_{min}$

Figure 5.

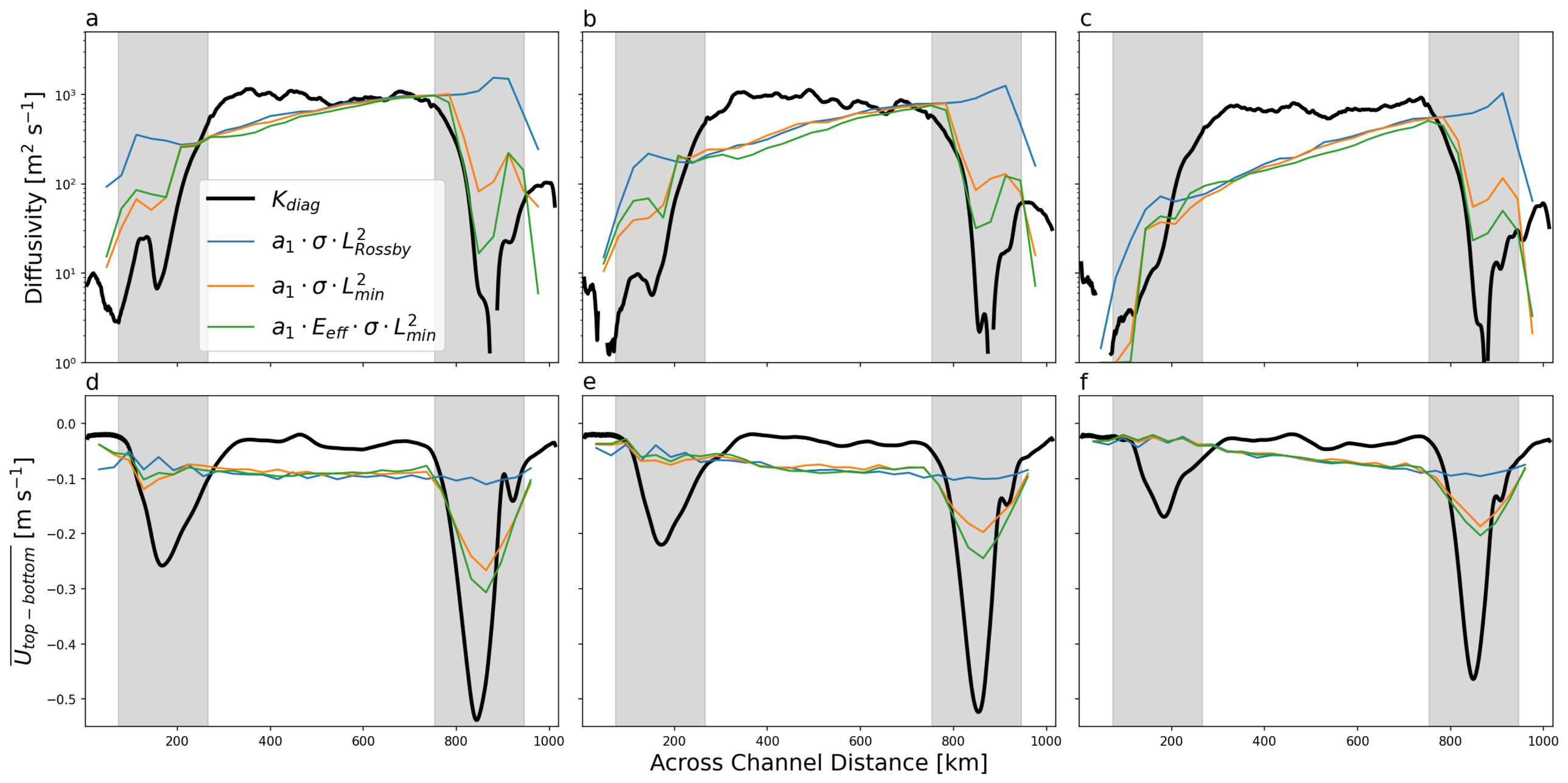
a
b
c
d
e
f
Diffusivity [m^2 s^{-1}]
$\overline{U_{top-bottom}}$ [m s^{-1}]
Across Channel Distance [km]
K_{diag}
$a_1 \cdot \sigma \cdot L^2_{Rossby}$
$a_1 \cdot \sigma \cdot L^2_{min}$
$a_1 \cdot E_{eff} \cdot \sigma \cdot L^2_{min}$
10^0
10^1
10^2
10^3
0.0
−0.1
−0.2
−0.3
−0.4
−0.5
200
400
600
800
1000

Figure 6.

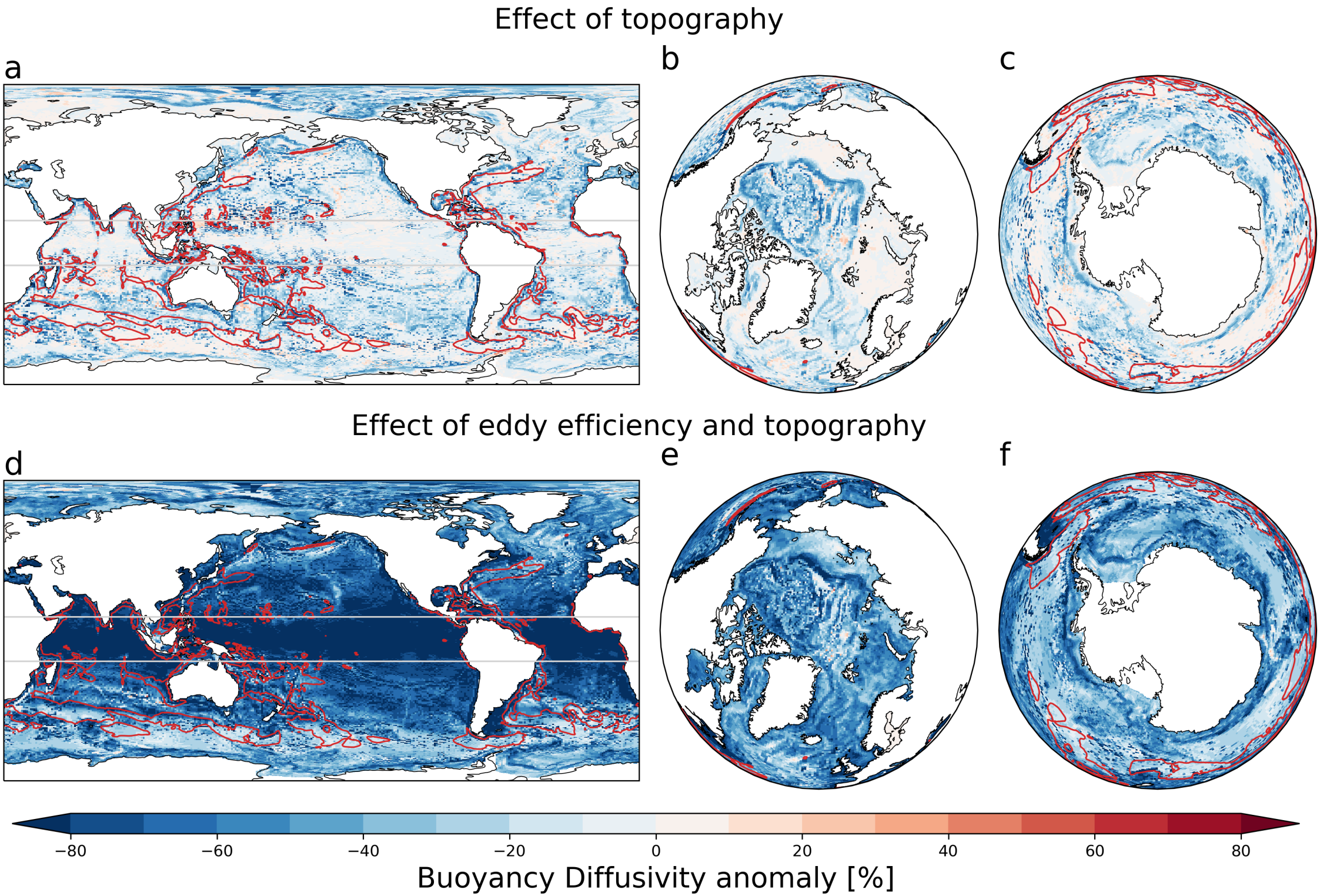
Effect of topography
a
b
c
Effect of eddy efficiency and topography
d
e
f
−80
−60
−40
−20
0
20
40
60
80
Buoyancy Diffusivity anomaly [%]

Figure 7.

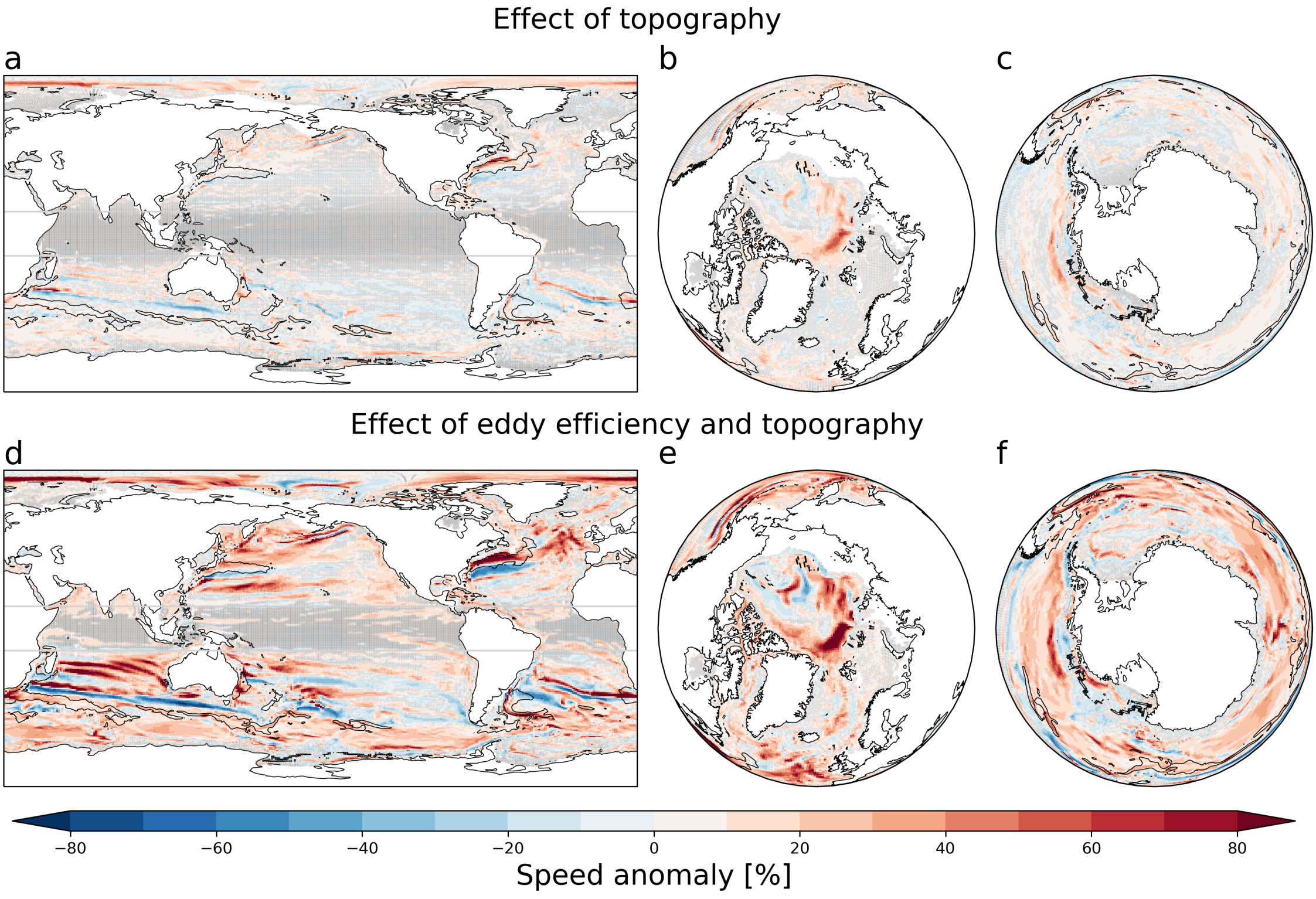
Effect of topography
a
b
c
Effect of eddy efficiency and topography
d
e
f
−80
−60
−40
−20
0
20
40
60
80
Speed anomaly [%]

Figure 8.

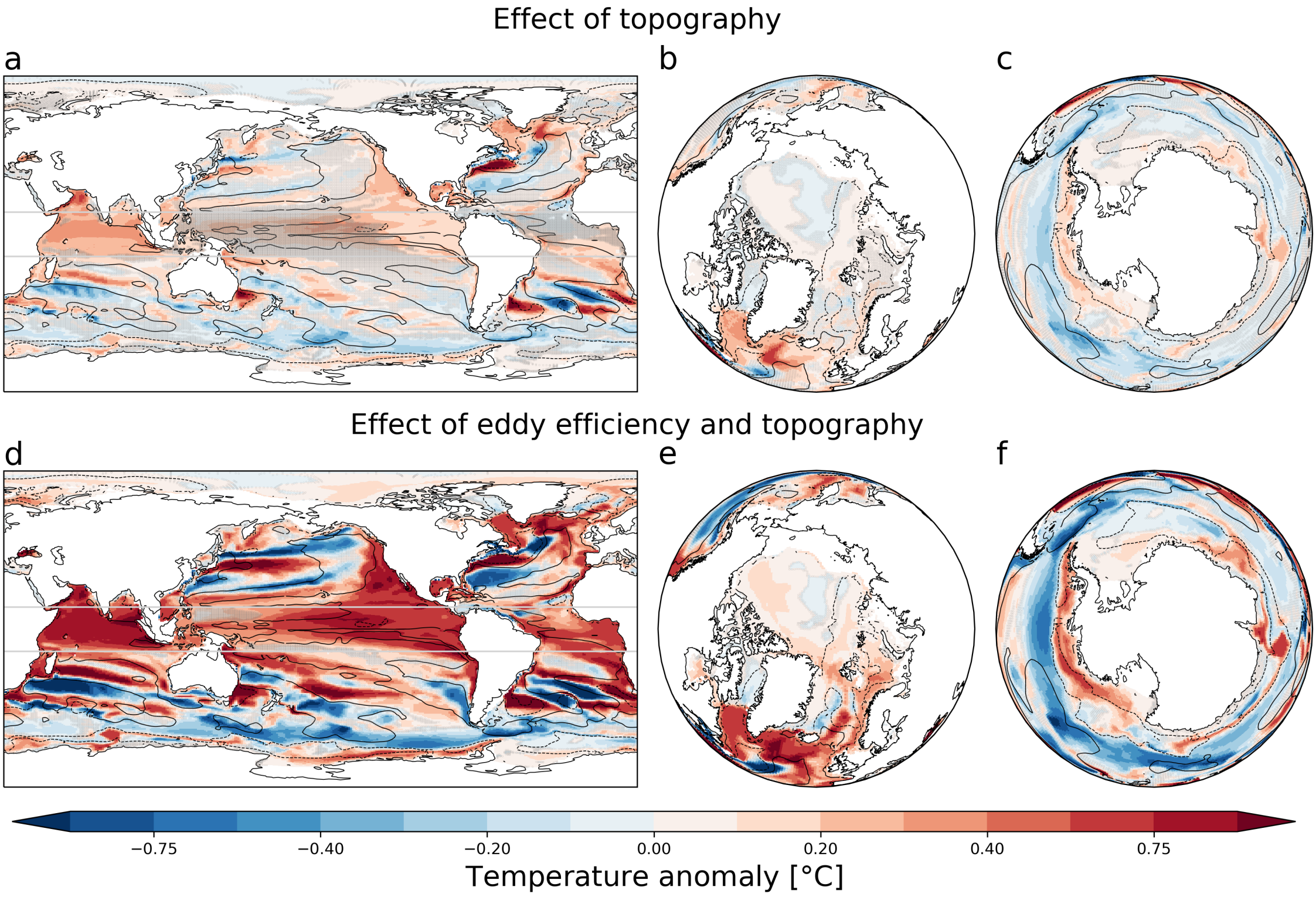
Effect of topography
a
b
c
Effect of eddy efficiency and topography
d
e
f
−0.75
−0.40
−0.20
0.00
0.20
0.40
0.75
Temperature anomaly [°C]

Figure 9.

Effect of topography

a

b

Effect of eddy efficiency and topography

c

d

Depth [m]

0
50
250
1000
2500
5000

−80 −60 −40 −20 0 20 40 60 80

Latitude [°N]

−0.9 −0.6 −0.3 0.0 0.3 0.6 0.9

Zonal Temperature anomaly [°C]

−5 −4 −3 −2 −1 1 2 3 4 5

MOC anomaly [Sv]

Figure 10.

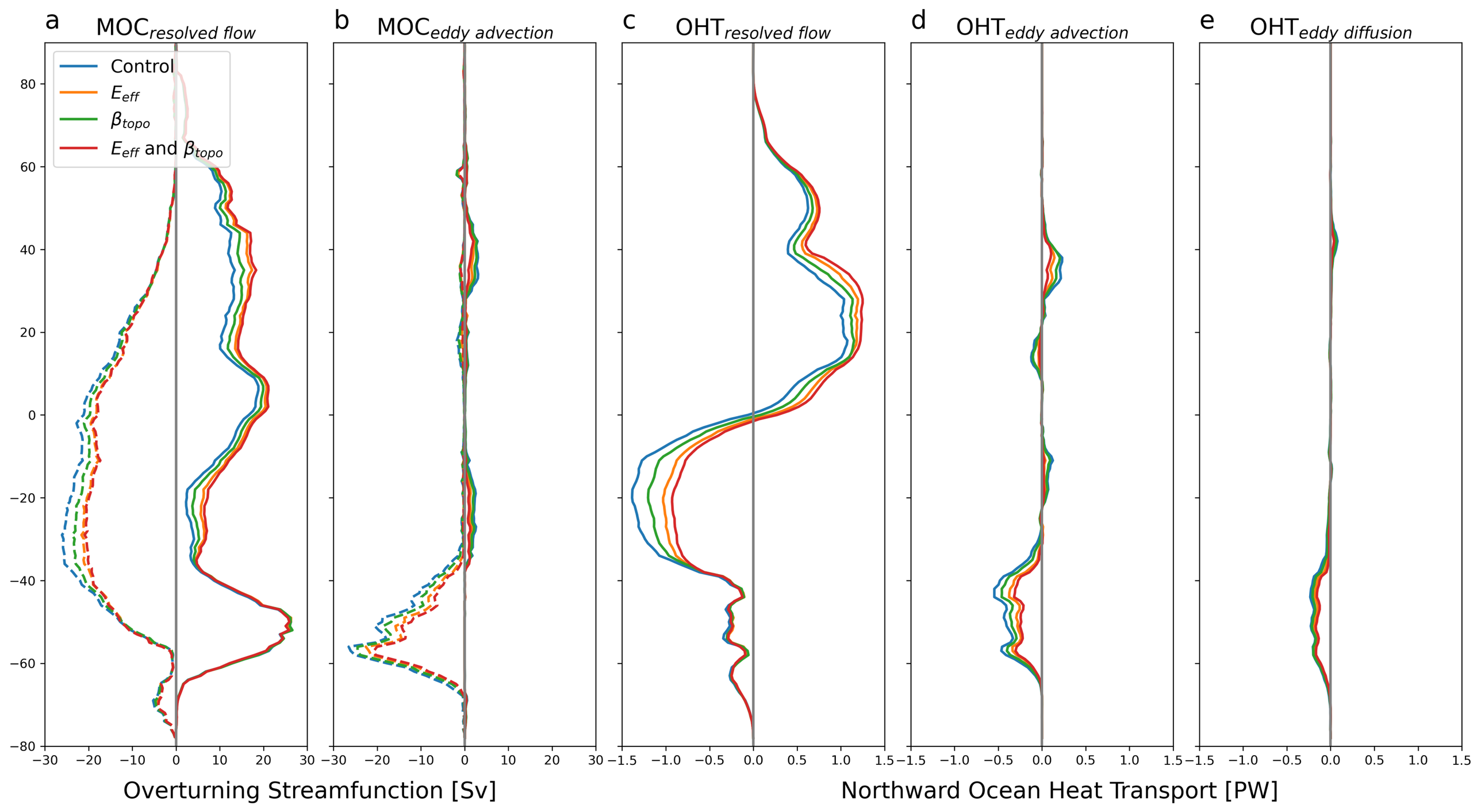
a
MOC resolved flow
b
MOC eddy advection
c
OHT resolved flow
d
OHT eddy advection
e
OHT eddy diffusion
Control
E_{eff}
β_{topo}
E_{eff} and β_{topo}
80
60
40
20
0
−20
−40
−60
−80
−30 −20 −10 0 10 20 30
−1.5 −1.0 −0.5 0.0 0.5 1.0 1.5
Overturning Streamfunction [Sv]
Northward Ocean Heat Transport [PW]